

Compact 2D-MOT and 3D-MOT Systems for Portable Quantum Gravimeter and Quantum Simulator

A Thesis

submitted to

Indian Institute of Science Education and Research Pune

in partial fulfillment of the requirements for the

BS-MS Dual Degree Programme

by

Vishal Lal



Indian Institute of Science Education and Research Pune

Dr. Homi Bhabha Road,
Pashan, Pune 411008, INDIA.

April, 2023

Supervisor: Prof. Dr. Umakant D. Rapol

© Vishal Lal 2023

All rights reserved

Certificate

This is to certify that this dissertation entitled Compact 2D-MOT and 3D-MOT Systems for Portable Quantum Gravimeter and Quantum Simulator towards the partial fulfilment of the BS-MS dual degree programme at the Indian Institute of Science Education and Research, Pune represents study/work carried out by Vishal Lal at Indian Institute of Science Education and Research under the supervision of Prof. Dr. Umakant D. Rapol, Professor, Department of Physics, during the academic year 2022-2023.

A handwritten signature in black ink, enclosed in a large, loopy oval. The signature appears to read 'U. D. Rapol'.

Prof. Dr. Umakant D. Rapol

Committee:

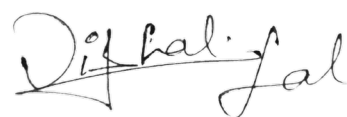
Prof. Dr. Umakant D. Rapol

Prof. Dr. Bhas Bapat

Dedicated to my *Family* and *Gurus*

Declaration

I hereby declare that the matter embodied in the report entitled Compact 2D-MOT and 3D-MOT Systems for Portable Quantum Gravimeter and Quantum Simulator are the results of the work carried out by me at the Department of Physics, Indian Institute of Science Education and Research, Pune, under the supervision of Prof. Dr. Umakant D. Rapol and the same has not been submitted elsewhere for any other degree.

A handwritten signature in black ink, appearing to read 'Vishal Lal', with a stylized, cursive script.

Vishal Lal

Acknowledgments

This was my first experimental experience in the field of Atomic Physics and Quantum Optics. I am grateful to my supervisor Prof. Dr Umakant D. Rapol for giving me a chance to work in the lab, and experience various state-of-the-art technologies and methods used in the development of quantum technology and precision measurement. Being a student of Prof. Dr Umakant D. Rapol has taught me various things professional and personal life. I thank him for his support and belief in me.

I would also like to thank my expert Prof. Dr Bhas Bapat for his valuable inputs to make the project more interesting.

The experimental and lab experience became even more memorable by working with seniors like Pranab Datta, Kushal Patel, Korak Biswas, Shiv Sagar Maurya and Rayees A.S. I thank them for the fruitful discussions and guiding me from the beginning of MS to the end.

Abstract

Cold atoms are extremely useful in a wide range of experiments, including atom interferometry, precision measurements, quantum simulation, and atomic clocks. The two-dimensional magneto-optical trap (2D-MOT) and three-dimensional magneto-optical trap (3D-MOT) act as cold atom sources.

A 2D-MOT confines the motion of the thermal atom from two dimensions by using near-resonant transition frequency laser beams exerting radiation pressure on the atoms in the light field. Because the atoms in this configuration are trapped only from two dimensions, they always have a velocity component in the third dimension, resulting in a cooling temperature of the order of μK . To get atoms down to a lower temperature, the cloud is transferred from a 2D-MOT to a 3D-MOT setup. A 3D-MOT setup is used to confine atoms in all three dimensions, resulting in temperatures lower than a 2D-MOT setup. In most laboratory-based setups, 2D-MOT is used as the first stage of cooling, and 3D-MOT is the second stage of cooling. The 3D-MOT experimental setup designed in this thesis loads the atom in the trap directly from the background vapour pressure of rubidium, and the number of atoms in the trap is 2.8×10^8 .

The goal of this thesis is to develop a platform for portable systems with better sensitivity outside the lab. Since these systems are the most commonly used systems for generating cold atoms, a compact design of these systems will result in a compact and portable design for Quantum Gravimeter and Quantum Simulator.

The setups were used to generate a cloud of cold atoms with a large number of atoms in the cloud, which was then characterised to determine the best operating conditions for the system. The 3D-MOT setup was then used for Electromagnetically Induced Transparency experiments of a *Ladder*-type system followed by spectroscopy of highly excited Rydberg state of ^{87}Rb . A *Ladder*-type system for excitation of the Rydberg state is used to generate an array of entangled neutral atoms for quantum information processing. The signal from the Rydberg spectroscopy was then used for frequency stabilisation of the coupling laser, also known as the Rydberg laser, used to excite the atom to a highly excited Rydberg state.

Contents

| | |
|--|-----------|
| Abstract | xi |
| 1 Introduction | 1 |
| 1.1 Atom Interferometers | 2 |
| 1.2 Neutral Atoms Array | 4 |
| 1.3 Objective of the Thesis | 5 |
| 1.4 Overview of the Thesis | 6 |
| 2 Laser Cooling and Trapping | 7 |
| 2.1 Light Matter Interaction | 7 |
| 2.2 Radiation Pressure Trap | 9 |
| 2.3 Magnetic Traps | 12 |
| 2.4 Optical Dipole Trap | 14 |
| 2.5 Cooling Methods | 21 |
| 2.6 Magneto-Optical Trap (MOT) | 31 |
| 2.7 Electromagnetically Induced Transparency | 34 |
| 2.8 Rubidium Atoms | 39 |

| | | |
|----------|---|-----------|
| 3 | Experimental Setup | 41 |
| 3.1 | Laser Frequency Stabilization | 41 |
| 3.2 | Two-Dimensional Magneto-Optical Trap | 46 |
| 3.3 | Three-Dimensional Magneto-Optical Trap | 50 |
| 3.4 | Experimental Setup of EIT | 55 |
| 4 | Experimental Results and Discussions | 57 |
| 4.1 | MOT Characterization | 57 |
| 4.2 | Fluorescence Images of Cloud of Cold Atoms. | 62 |
| 4.3 | Electromagnetically Induced Transparency. | 62 |
| 5 | Summary and Outlook | 67 |
| 5.1 | Summary | 67 |
| 5.2 | Future Outlook | 68 |

Introduction

Quantum mechanics underpins current physics, science, and technology. Since its inception one hundred years ago, quantum mechanics has been utilised to make remarkable predictions about nature, and experimental verification of these predictions has elevated quantum mechanics to the ranks of the most successful physics theories. While quantum theory supports our understanding of the macroscopic world, it also provides counterintuitive predictions about nature: concepts like quantum superposition and entanglement contradict conventional intuition and are, in fact, impossible to witness in normal conditions. These properties must be studied in exotic regimes to experience these phenomena: at ultracold temperatures or in carefully isolated, ultra-high vacuum conditions. As a result, specifically built systems are always required to subject atoms to such extreme environments.

The experimental realisation of such a system is difficult due to the requirement of extreme environments and the use of precise control systems to manipulate atoms; however, the complex nature of interaction in the quantum mechanical regime makes the field unpredictable and motivates new experiments in the field. Technological advancements have resulted in the development of a compact and user-friendly method for producing cold atoms.

Decades of research with cold atoms have made them one of the most promising candidates for use in the development of quantum technologies. Cold atoms have been employed in the Atom Interferometer to measure gravity and other forces in nature, in atomic clocks, and in the Quantum Simulator to simulate the behaviour of complicated quantum systems and quantum information processing. This thesis aims to develop a compact and user-friendly

which can serve as a platform for a portable cold atom system ready for field deployment.

1.1 Atom Interferometers

The acceleration due to gravity (g) is a local quantity that varies with time and is dependent on local factors. Its value is significant in many scientific domains, including geophysics, geology, and metrology [9]. Accurate measurement of g has several applications in defence, such as tunnel detection and inertial navigation, as well as in the exploration of gas, oil, water and other natural resources.

The value of g is significant in metrology because most force measurements use the weight of a known mass as a reference, which is only possible if the value of g is known with great precision. Other quantities like temperature, current, and pressure are characterised using these force measurements.

Geophysical applications mostly include geographic mapping in g variations to acquire information about the spin, composition, and shape of the Earth. The minimum accuracy for these applications ranges in the order of 10^{-6} to 10^{-8} m/s^2 . Some applications, such as tides and crustal deformations, need the analysis of time-dependent fluctuations in g with greater than 10^{-8} m/s^2 accuracy.

Instruments that measure gravity are called gravimeters and are classified into two categories: relative gravimeters and absolute gravimeters.

Relative gravimeters are spring-based instruments that support a test mass against gravity using a well-characterized spring. Even minor changes in gravity cause noticeable differences in the length of the spring. These instruments have an accuracy of 10^{-9} m/s^2 while remaining compact and portable, making them suitable for geophysical and geological applications. Nevertheless, the reading is a relative quantity, which is the difference between the gravity measurement of a known location and the relevant site, and these gravimeters drift significantly, thus, they must be calibrated regularly before measurements to get maximum accuracy. Cryogenic gravimeters outperform all other instruments in terms of noise performance [23, 25]. They are, in many ways, an enhanced variant of spring-type gravimeters. It employs a superconducting sphere that is levitated in a magnetic field, and it uses force

feedback mechanisms to counteract for variations in gravity. When compared to spring-type gravimeters, the drift rate is less and better. These gravimeters are more sophisticated than spring-based gravimeters. They are more susceptible to vibrations, which translates into gravity measurements, rendering them unsuitable for transporting and measuring the gravity of different locations.

Absolute gravimeters are required for a variety of applications that exceed the capability of relative instruments. In applications where absolute gravity values must be measured, this includes comparing gravity measurements taken at different points in space and time. A classical method approach for measuring gravity is to use a pendulum, although this method is time-consuming and has an accuracy limit of roughly 10^{-7} m/s². Contemporary gravimeters employ a laser interferometer to measure the velocity of an object, often a corner-cube retro-reflector, and have an accuracy of $\sim 2 \mu\text{Gal}^1$ [16]. Even falling corner-cube gravimeters have space for development since their noise levels are higher than relative gravimeters. One of the primary causes of significant noise is that the measurement is not continuous.

The idea of building a matter-wave interferometer out of neutral atoms has been around for quite some time. It was ultimately accomplished in 1991. The performance of atom interferometers has significantly increased since 1991. They have progressed to the point where they are no longer merely examples of quantum mechanics. Instead, they may now be used as tools to make a wide range of important measurements with precision and accuracy that challenges and outperforms any competitive equipment. The approaches pioneered by Kasevich, Chu, and Peters at Stanford have been particularly effective in this regard. An atom interferometer works similar to modern laser interferometers, which are based on Mach-Zehnder interferometer configuration, where a laser beam is split into two with the help of a beamsplitter into two arms of Mach-Zehnder interferometer, one arm of the interferometer is fixed while the other arm is the falling corner-cube retro-reflector and the motion of this corner-cube is measured by the change in interference pattern due to change in optical path length of the arm of Mach-Zehnder interferometer which is due to gravity. An atom interferometer uses matter-wave instead of light waves. And light wave act as beamsplitters and mirrors in atom interferometers. The technique uses precisely tailored laser beam pulses for coherent transfer of atom population to the hyperfine ground state, one such technique was developed by Kasevich and Chu [16].

¹ μGal is the unit for precision gravity measurement. $1 \mu\text{Gal} = 10^{-6} \text{ cm/s}^2 = 10^{-8} \text{ m/s}^2 \approx 10^{-9} \text{ g}$

1.2 Neutral Atoms Array

The intricate nature of the interaction and evolution of quantum systems makes them difficult to investigate, and in certain situations, the systems are too complicated that they cannot be studied. Richard Feynman proposed a solution to this challenge in 1982, which was to create a toy model of a quantum system that could be programmed to simulate the behaviour and evolution of such a system [11]. Since then, various platforms for the system, including trapped ions and arrays of neutral atoms, have been developed, and this idea was termed as Quantum Simulator. Because these systems evolve in unpredictable ways, can we design them so that their evolution results in answers to a given computational question? This is the concept of quantum information processing or quantum computing, in which quantum mechanical systems solve traditional computational problems.

Neutral Atoms have become a prominent choice for Quantum Simulators and Quantum Computers due to their great scalability in terms of the number of qubits, efficient error correction when Rydberg atoms interact on demand, and flexibility in array arrangement.

Experiments are carried out in ultra-high vacuum chambers using a well-developed toolkit of lasers, microwaves, and magnetic fields to manipulate atoms. Each experiment starts with the laser cooling of millions of identical atoms in a magneto-optical trap (MOT). Atoms are subsequently put into optical tweezers, which are lasers with tightly focused focal points that produce trapping potentials. The number of optical tweezers that can be generated determines the accessible system sizes that can be explored using this method. Current systems are capable of producing hundreds, if not thousands, of tweezers, and merely increasing the available laser power allows for scalability to much bigger arrays. The optical tweezers platform has advantages from short experimental cycle durations and relative ease of use. The method of loading atoms from the MOT into the optical tweezers, however, is stochastic; after each loading attempt, each tweezer will be randomly loaded with a single atom with a probability of 0.5. After initialising a target atom array, atoms can be stimulated to highly excited atomic states known as Rydberg states to establish strong and controllable interactions [5, 20, 28]. Rydberg interactions produce a complex quantum spin model with several quantum phases that originate from the conflict between interactions and coherent driving. These interactions may also be used to allow a variety of quantum information and entanglement-generating processes.

The technological capabilities of neutral atom systems based on tweezer arrays have advanced dramatically during the last many years. Hundreds of atoms in two and three spatial dimensions may now be easily trapped and arranged inside such tweezer arrays [2, 8, 22]. It has been proven that coherent excitation to Rydberg states and high-fidelity quantum operations are possible.

1.3 Objective of the Thesis

The previous sections' experiments and methodologies are carried out in ideal laboratory circumstances using large, complicated systems. The purpose of this thesis is to develop a portable two-dimensional magneto-optical trap (2D-MOT) and three-dimensional magneto-optical trap (3D-MOT) that can be utilized in field applications. The thesis first discusses designing and developing compact systems. This involves the vacuum assembly, which is a major factor in determining the size of the system, as well as the simulation and design of quadcoils that generate a quadrupolar magnetic field. This magnetic field is important for the system because it provides a restoring force on atoms and also makes light absorption by atoms a position-dependent phenomenon, which plays a critical role in laser cooling, and designing an optical layout with the least components and space to make the system robust and compact, as well as discussing some of the ways to optimise the parameter and optical alignment for trapping the most atoms with the least amount of power in laser beams and magnetic coils.

Once the system was ready for MOT, experiments were carried out in it, including the observation of Electromagnetically Induced Transparency (EIT) for a *ladder*-type system, confirming the formation of Rydberg atoms in MOT, and spectroscopy of the Rydberg state to calculate the linewidth of the excited Rydberg state. The frequency of the Rydberg state excitation laser was finally locked and stabilised using this signal.

1.4 Overview of the Thesis

Chapter 2 discusses the theoretical foundation of laser cooling as well as laser cooling techniques such as Doppler Cooling and Sub-Doppler Cooling. This Chapter includes a discussion on traps such as Far Detuned Dipole Traps and Magnetic Traps, as well as a brief theoretical background on Electromagnetically Induced Transparency (EIT) and Rydberg states. Finally, the chapter discusses imaging of MOT for estimating the number of atoms, decay rate, and loading rate of the MOT.

Chapter 3 provides a detailed description of the experimental setup of 2D-MOT and 3D-MOT used to generate a cloud of cold ^{87}Rb atoms.

The 2D-MOT setup consists of a quartz glass cell of dimension $40 \times 40 \times 140$ mm, and pressure inside the glass cell is 10^{-9} Torr. A rubidium oven attached to the glass cell operating at 40°C is the source of thermal atoms. And two pairs of rectangular coils in an anti-Helmoltz configuration to generate the required magnetic field for the trap.

For the 3D-MOT setup, a stainless steel chamber is used as the science chamber to hold the pressure of 8.5×10^{-10} Torr inside the chamber. A pair of circular coils operating at 6 A in an anti-Helmoltz configuration generates the magnetic field with a constant magnetic field gradient of 17.85 G/cm. And a rubidium oven operating at 45°C is the source for thermal atoms.

The 3D-MOT setup was then used for EIT experiments. The cooling laser was used as the probe laser, and a coupling laser was aligned to pass through the centre of the cloud of cold atoms trapped in the 3D-MOT.

Chapter 4 describes the detection and characterisation of a cloud of cold atoms in the MOT, as well as electromagnetically induced transparency and Rydberg spectroscopy in the MOT.

Chapter 5 summarises the work done in this thesis and provides an outlook for future experiments.

Laser Cooling and Trapping

The technique of optical cooling and trapping of neutral atoms is one of the most successful and elegant experimental method used in atomic physics. It is preferred widely due to its ability to slow down velocity of atoms, reducing the kinetic energy of the atoms, resulting in reduced collisional perturbation, providing long interaction time, and trap a large number of atoms at sufficiently high density. These characteristics make the cold atom a promising platform for various precision experiments in areas like quantum optics, coherent phenomena, atomic clock and frequency standards, cold collisions, atom interferometer and atom optics. In 1975, T. Hänsch and A. Schawlow proposed the use of laser light to slow down atoms [14], which was later realized in the 1980s by W. Phillips and H. Metcalf, demonstrating the use of laser light to stop an atomic beam [24]. Following, Chu et al. demonstrated optical molasses (OM) [6], and Raab et al. demonstrated the magneto-optical trap (MOT) at Bell Laboratories [26]. The fundamental principle behind using laser light to stop atoms is light-matter interaction.

2.1 Light Matter Interaction

Maxwell's classical theory of electromagnetic radiation predicted the force of radiation on matter, which was proved experimentally at the beginning of the twentieth century [12]. A comprehensive analysis of light-matter interactions was successfully explained using the

Bohr model of the atom and Einstein's theory of atomic absorption, spontaneous emission and stimulated emission of the radiation field. To understand light-matter, we shall use a Semi-classical approximation treatment on a two-level atom in an Electromagnetic field.

In Semi-classical approximation treatment, a classical electromagnetic field interacts with a quantum atom. When an atom interacts with an electromagnetic field in the strong field limit. The probability of finding an atom in the ground and excited states are given by:

$$|c_1(t)|^2 = \cos^2\left(\frac{\Omega_R t}{2}\right) \quad (2.1)$$

$$|c_2(t)|^2 = \sin^2\left(\frac{\Omega_R t}{2}\right) \quad (2.2)$$

where $|c_1(t)|^2$ and $|c_2(t)|^2$ are the probabilities of finding an atom in the ground state and excited, respectively, and Ω_R is the Rabi Frequency. The population of atoms in excited and ground states oscillate as shown by Eq. 2.1 and Eq. 2.2. This Oscillatory behaviour in response to strong-field is called Rabi Oscillation or Rabi Flopping and the frequency of this oscillation is called Rabi Frequency. Due to the presence of light, an additional interaction energy term gets added to the Hamiltonian, and the atomic energy levels of the atoms are shifted. This is referred to as "light shift" or "AC Stark shift". The shift in energy levels is given by:

$$\delta E_{light} = \frac{\hbar \Omega_R^2}{4\Delta} \quad (2.3)$$

where Ω_R is Rabi Frequency, and $\Delta = \omega_{light} - \omega_0$ is the detuning of the light frequency from the atomic resonance frequency ω_0 . For a red-detuned light ($\Delta < 0$), using the dipole approximation and $|\Delta| \gg \Gamma$ (Γ being the natural linewidth of the transition of upper level or excited state of the two-level atomic system), energy shift is positive for excited state and negative for the ground state.

Traps for neutral atoms can be generated by three main interactions, each with its own set of traits and advantages:

- *Radiation Pressure Trap*
- *Magnetic Trap*
- *Optical Dipole Trap*

2.2 Radiation Pressure Trap

A ***Radiation Pressure Trap*** can be made by using near-resonant light, which generally possesses a few Kelvin depths and is capable of trapping thermal atoms emitted from an oven due to its high dissipation. This trap can cool the atomic ensemble to a few tens of micro-Kelvin. According to Einstein's theory, light is quantized by photons or quanta that possess energy $E = h\nu$ and momentum $\vec{p} = \hbar\vec{k}$, where ' ν ' represents frequency, and the wave vector of light with a wavelength λ is $|k| = 2\pi/\lambda$. Upon the absorption of a photon, momentum is transferred to the atom while preserving its magnitude and direction in line with the principle of momentum conservation demonstrated in Fig. 2.1. This leads to a small momentum kick that modifies an atom's velocity by recoil velocity $v_{rec} = \hbar k/M \approx 1$ cm/s (e.g., 0.6 cm/s for an Rb atom), which can be compared to normal speeds of a few 100 m/s in atoms at room temperature. After absorption, spontaneous emission occurs with a natural lifetime $\tau = 1/\Gamma_e$ of the excited state, where Γ_e is the decay rate (or width), causing the atom to recoil once more. Since spontaneous emission is isotropic, the recoil of the atom associated with this process is random, resulting in no net change in momentum on average. Therefore, absorption is primarily responsible for the total change in atomic momentum, as illustrated in Fig. 2.1. The force $F = d\vec{p}/dt$ exerted on an atom is directed along the laser beam and increases in proportion to the incoming light's intensity until stimulated emission starts to take effect. While higher intensity induces quicker absorption, it also amplifies stimulated emission. The stimulated emission photon travels in the same direction as the stimulating photon. Consequently, the momentum transfer during stimulated emission is directed in the opposite direction to the momentum transfer during absorption. As a result, the overall change in atomic momentum in such a sequential cycle is zero. As the atom spends half of its time in each of the states under a high-intensity beam, $f_{max} = 1/2$, the resulting acceleration cannot exceed $\vec{a}_{max} = \hbar\vec{k}f\Gamma_e/M$ (where M is the mass of the atom and f is the time atom spends in an excited state) [17].

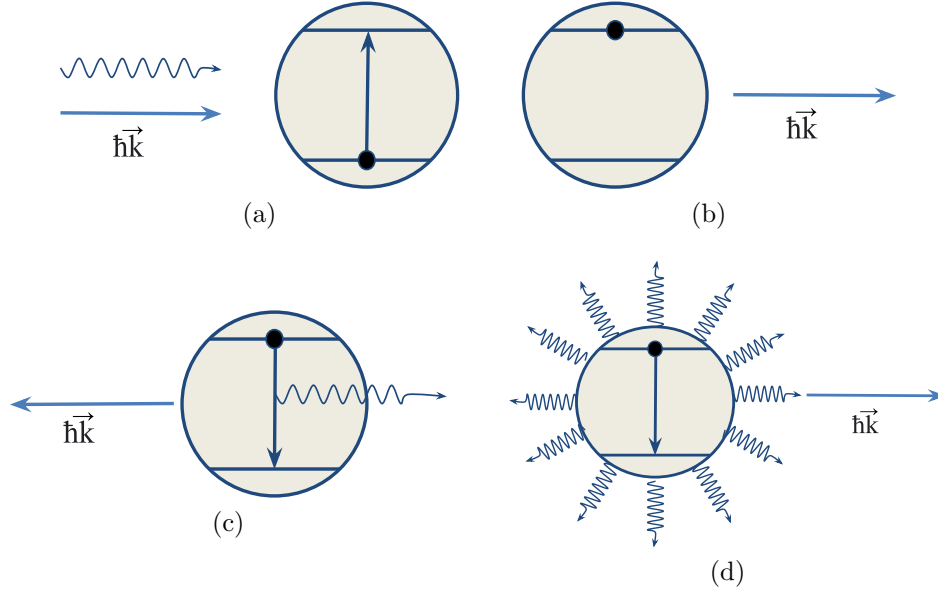


Figure 2.1: The interaction of a two-level atom with resonant light involves several steps. In (a), a photon that is resonant with the atomic transition approaches the atom in its ground state. After being absorbed by the atom in (b), the atom excites to the excited state and gains momentum in the direction of the wavevector of the photon, which is given by $\hbar\vec{k}$. In (c), the excited atom emits a single photon, causing a momentum recoil in the opposite direction of $\hbar\vec{k}$. Finally, the net change in atomic momentum due to isotropic spontaneous emission, which is averaged over multiple absorption and emission cycles, is *zero*, as shown in (d).

When a light beam is present, the change in momentum or net force on the atom is produced after several scattering events in the direction of the propagating light beam. As a result, in the presence of a light beam, the scattering force on an atom is given by the rate at which momentum is transferred to the atom:

$$F_S = \hbar k R_S \quad (2.4)$$

where R_S is the Scattering rate of the atom, given by:

$$R_S = \frac{\Gamma}{2} \frac{\Omega_R^2/2}{\Delta^2 + \Omega_R^2/2 + \Gamma^2/4} = \frac{\Gamma}{2} \frac{I/I_{Sat}}{1 + I/I_{Sat} + 4\Delta^2/\Gamma^2} \quad (2.5)$$

where I is the light intensity and I_{Sat} is the saturation intensity of the transition, defined

as the intensity at which the transition is power broadened by a factor of $\sqrt{2}$, and is given by:

$$I_{Sat} = \frac{h\nu}{2\tau(3\lambda^2/2\pi)} \quad (2.6)$$

Δ is the detuning for the incident light frequency from the atomic resonance frequency and Γ is the natural linewidth of the transition, τ is the lifetime of the excited state, and ν is the transition frequency.

Eqs. 2.4 and 2.5 show that the scattering force is Lorentzian. The maximum scattering force experienced by the atom is given by $\hbar k\Gamma/2$ for zero detuning and intensity I considerably greater than I_{Sat} . For ^{87}Rb , the natural linewidth (FWHM) of the $5^2S_{1/2} \longleftrightarrow 5^2P_{3/2}$ transition is $\Gamma = 2\pi \times 6.1$ MHz, and the saturation intensity at 780 nm is 1.6 mW/cm².

The strong optical excitation, however, limits trap performance in several ways: limitations on achievable temperature due to photon recoil, limitations on achievable density due to radiation trapping and light-assisted inelastic collisions, and perturbations to internal dynamics caused by resonant processes on a microsecond timescale. Scattering force is significant when the linewidth of the laser beam is narrower than the natural linewidth. With the development of narrow-band tunable lasers in the 1970s, it became possible to generate light profiles that meet this requirement.

To optically trap an atom, lasers must be provided with a restoring force towards the trap equilibrium point whenever the atom is moved from that point. The objective is to devise a method that forces the atom to interact strongly with a laser beam that opposes its motion.

There are various techniques that might do this; they are classified into two categories. The first class uses external influence, such as a magnetic field, to control the atom's affinity for a particular light. For example, the magnetic field can be used to Zeeman tune the atom's resonance frequency or to shift its quantisation axis. The second class is based on unusual optical pumping phenomena observed in particular atoms, such as cesium. Because of these effects, the atom absorbs more photons from a preferred beam, even if it is less powerful than a competing beam of opposite polarisation.

2.3 Magnetic Traps

Magnetic traps exploit the state-dependent force on the magnetic dipole moment in a non-uniform magnetic field. They are useful for evaporative cooling and Bose-Einstein condensation since they are conservative traps that can achieve depths of the order of 100 mK. The interest in magnetic trapping of atoms is motivated by the dynamics and stability of the trap itself, as well as the potential applications of trapped atoms, including measuring long metastable-state lifetimes, cooling atoms to extremely low temperatures of few micro-Kelvins, and study of quantum collective effects at low temperature and high density [21]. Ultrahigh-resolution spectroscopy without motional Doppler or transit-time effects could be performed on extremely cooled atoms released from the trap, and in some cases, spectroscopy could be carried out on atoms still trapped within the trap.

Since an inhomogeneous magnetic field exerts forces on atoms having magnetic dipole moments, magnetic trapping is possible [21]. Atoms in quantum states with increasing energy are trappable, and if the Zeeman energy increases linearly, the potential energy equals the effective magnetic moment μ multiplied by the magnitude of the magnetic field B . Potential experienced by atoms in an inhomogeneous magnetic field is given by:

$$U(F, m_F) = -g_F m_F \mu_B |B| \quad (2.7)$$

where g_F is Lande g factor, Hence states with $g_F m_F < 0$ are magnetically trappable states. For example, in the case of ^{87}Rb , the three low-field seeking states are $|F = 2, m_F = 2\rangle$, $|F = 2, m_F = 1\rangle$, and $|F = 1, m_F = -1\rangle$. As a result, atoms become trappable in one of these states.

2.3.1 Spherical Quadrupole Trap

A spherical quadrupole trap is one of the simplest magnetic traps, and it is constructed using a pair of coils in an "anti-Helmholtz" configuration, in which the currents are oriented in opposing directions. This trap produces an axially symmetric magnetic field that is linear around the coils' centre. The Magnetic field near centre for the coil is

$$\mathbf{B} = B'_z z \mathbf{e}_z + \frac{1}{2} B'_x x \mathbf{e}_x + \frac{1}{2} B'_y y \mathbf{e}_y \quad (2.8)$$

where axial and radial gradients are related as:

$$B'_z = \frac{\partial B}{\partial z} = 2 \frac{\partial B}{\partial r} = 2B'_r \quad (2.9)$$

The magnetic field of a spherical quadrupole has a minimum value equal to zero, which is at the centre of the trap. The magnetic moment of the atoms constantly precesses around the local magnetic field with a frequency equal to Larmor frequency ω_{Larmor} , given by:

$$\omega_{Larmor} = \frac{g_F m_F \mu_F}{\hbar} |B| \quad (2.10)$$

The local magnetic field observed by the atoms in a magnetic trap constantly changes as the atom travels within the trap. Only when the change in the local magnetic field is adiabatic with respect to the Larmor frequency, the atom can be trapped. Consequently, for trapping, the Larmor frequency must be significantly greater than the variation rate of the angle ϕ of the magnetic field realised in the atomic frame, i.e.

$$\frac{d\phi}{dt} \ll \omega_{Larmor} \quad (2.11)$$

When the temperature is very low, and the density is very high in a spherical quadrupole trap, the adiabatic condition is violated because the magnetic field is zero at the centre ($|B| = 0$). When atoms approach the trap centre, the separation between the Zeeman sub-levels becomes very narrow, and the atom has a very high probability of transitioning into untrapped states, known as "Majorana spin flips," resulting in loss of atom from the trap. Majorana spin flips have an effective rate of $\sqrt{2\hbar\nu/\pi\nu B'}$. As a result, an additional magnetic field is required to achieve a non-zero field minimum in order to remove the Majorana spin flips. Magnetic traps are classified into two types: Ioffe-Pritchard (IP) traps and Time-averaged orbiting potential (TOP) [18].

The fact that the trapping process is dependent on the internal atomic state imposes a

fundamental constraint. This means that experiments on internal dynamics are restricted to a few particular instances. Additionally, viable trapping geometries are limited by the requirement to use coil or permanent magnet configurations.

2.4 Optical Dipole Trap

Optical dipole traps are created using far-detuned light that interacts with the electric dipole of the atom. The strength of the interaction is much weaker than other trapping methods described earlier. On average, the depth of the trap is less than one millikelvin. The amount of optical excitation required for the trap is extremely low, which makes it independent of the light-induced processes seen in radiation pressure traps. The trapping process is not affected by the specific sub-level of the electronic ground state in certain circumstances. Therefore, it is possible to conduct experiments utilizing the ground-state dynamics over a time scale of several seconds [13].

2.4.1 Optical Dipole Potential

A Oscillator Model

The dispersive interaction between the induced dipole moment of an atom and the intensity gradient of a light field leads to the optical dipole force. This force is conservative in nature, hence, can be derived from a potential, making it suitable for trapping the atoms. However, with far-detuned light, residual photon scattering due to the absorptive component of the dipole interaction can limit the performance of these traps.

When an atom is exposed to laser light, the electric field E produces an atomic dipole moment p , oscillating at the driving frequency ω . And Electric field and dipole moment is given by:

$$\mathbf{E}(r, t) = \hat{e}\tilde{E}(r)\exp(-i\omega t) + c.c \quad (2.12)$$

$$\mathbf{p}(r, t) = \hat{e}\tilde{p}(r)\exp(-i\omega t) + c.c \quad (2.13)$$

where \hat{e} is the unit polarization vector. And amplitude of the dipole moment \tilde{p} is related to amplitude of electric field \tilde{E} as:

$$\tilde{p} = \alpha \tilde{E} \quad (2.14)$$

where α is *complex polarizability* and depends on driving frequency ω . The *interaction potential* of the induced dipole is given by:

$$U_{Dip} = -\frac{1}{2} \langle \mathbf{p} \mathbf{E} \rangle = -\frac{1}{2\epsilon_0 c} \text{Re}(\alpha) I \quad (2.15)$$

where the angular brackets represent the time average over the rapid oscillating phases, the field intensity is $I = 2\epsilon_0 c |\tilde{E}|^2$. The 1/2 factor is included in the formula to adjust for the fact that the dipole moment is not permanent, but rather induced. The potential energy of the atom within the field is proportional to the intensity I and the real component of the polarisability of the trapping laser, which reflects the in-phase component of the dipole oscillation and drives the dispersive nature of the interaction. The dipole force produced is due to the gradient of the interaction potential.

$$\mathbf{F}_{Dip} = -\nabla U_{Dip} = \frac{1}{2\epsilon_0 c} \text{Re}(\alpha) \nabla I(\mathbf{r}) \quad (2.16)$$

Power absorbed by the oscillator from the driving field is:

$$P_{abs} = \langle pE \rangle = 2\omega \text{Im}(\tilde{p} \tilde{E}^*) = \frac{\omega}{\epsilon_0 c} \text{Im}(\alpha) I \quad (2.17)$$

The absorption of light by an atom is caused by the imaginary part of its polarisability, which represents the out-of-phase component of the dipole oscillation. This occurs because the atom interacts with light as a stream of photons with energy $\hbar\omega$, and during absorption cycles, the photons are scattered during absorption and then re-emitted spontaneously. This process results in a scattering rate given by:

$$\Gamma_{sc}(r) = \frac{P_{abs}}{\hbar\omega} = \frac{1}{\hbar\epsilon_0 c} \text{Im}(\alpha) I(\mathbf{r}) \quad (2.18)$$

The complex polarisability α is given as

$$\alpha = 6\pi\epsilon_0 c^3 \frac{\Gamma/\omega_0^2}{\omega_0^2 - \omega^2 - i(\omega^3/\omega_0^2)\Gamma} \quad (2.19)$$

where ω_0 is on-resonance frequency and Γ is the damping rate given by:

$$\Gamma = \frac{\omega_0^3}{3\pi\epsilon_0 \hbar c^3} |\langle e | \mu | g \rangle|^2 \quad (2.20)$$

For the case of Large detunings and negligible saturation Eqs. 2.15 and 2.18 change to:

$$U_{Dip}(r) = -\frac{3\pi c^2}{2\omega_0^3} \left(\frac{\Gamma}{\omega_0 - \omega} + \frac{\Gamma}{\omega_0 + \omega} \right) I(\mathbf{r}) \quad (2.21)$$

$$\Gamma_{sc}(r) = \frac{3\pi c^2}{2\hbar\omega_0^3} \left(\frac{\omega}{\omega_0} \right)^3 \left(\frac{\Gamma}{\omega_0 - \omega} + \frac{\Gamma}{\omega_0 + \omega} \right)^2 I(\mathbf{r}) \quad (2.22)$$

Experiments often tune the laser frequency near the atomic resonance frequency ω_0 , with the detuning $\Delta = \omega - \omega_0$ satisfying the condition $|\Delta| \ll \omega_0$. This approximation allows for neglecting the counter-rotating term in the rotating-wave approximation and using $\omega/\omega_0 \approx 1$ simplifies Eqs. 2.21 and 2.22 to:

$$U_{Dip}(r) = \frac{3\pi c^2}{2\omega_0^3} \frac{\Gamma}{\Delta} I(\mathbf{r}) \quad (2.23)$$

$$\Gamma_{sc}(r) = \frac{3\pi c^2}{2\hbar\omega_0^3} \left(\frac{\Gamma}{\Delta} \right)^2 I(\mathbf{r}) \quad (2.24)$$

Eqs. 2.23 and 2.24 explain the basic physics of a far-detuned dipole trap. And the relation between scattering rate and dipole potential is:

$$\hbar\Gamma_{sc} = \frac{\Gamma}{\Delta} U_{Dip} \quad (2.25)$$

This is a direct result of the oscillator’s fundamental relationship between absorptive and dispersive response. Eqs. 2.23 and 2.24 also lead to the following conclusions.

- *Sign of Detuning:* when the dipole potential is negative below an atomic resonance (“red” detuning, $\Delta < 0$), the interaction attracts atoms into the light field. Potential minima are thus found at maximum-intensity sites. The dipole interaction repels atoms out of the field above resonance (“blue” detuning, $\Delta > 0$), and potential minima correspond to intensity minima as shown in Fig. 2.2. Dipole traps are classified into two types based on this distinction: red-detuned traps and blue-detuned traps.
- *Scaling with intensity and detuning:* The dipole potential scales as I/Δ , but the scattering rate scales as I/Δ^2 due to intensity and detuning. As a result, optical dipole traps often use large detunings and high intensities to keep scattering rates as low as possible for a given potential trap depth.

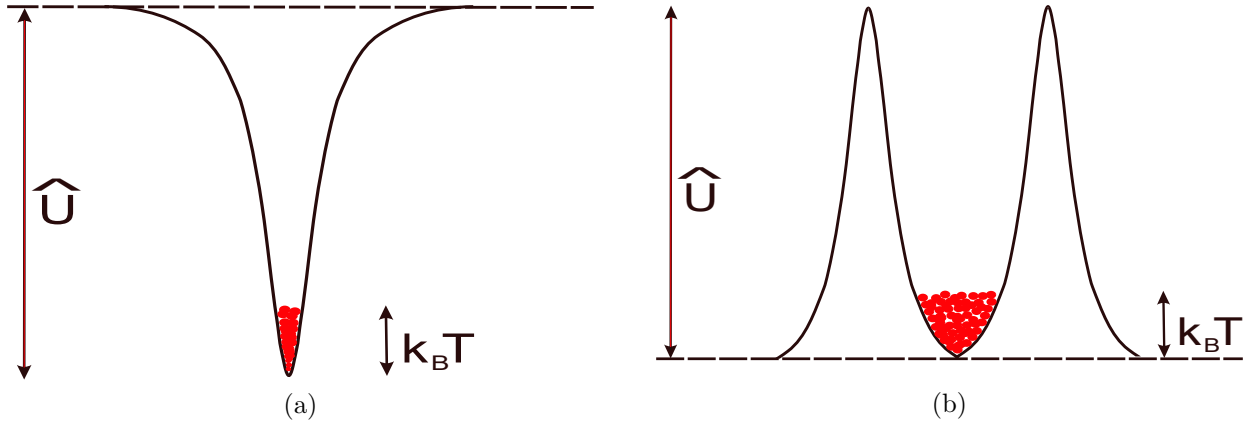


Figure 2.2: Dipole Trap Potential. (a) Gaussian beam creates a red-detuned trap at the minima of potential. (b) Laguerre-Gaussian LG_{01} beam creates a blue-detuned trap at the minima of the potential.

2.4.2 Multi-Level Atom

In the preceding section, the fundamental formulation of an optical dipole trap was derived using a simplified model with a two-level system. However, Atoms have multiple energy levels. As a result, all atomic energy levels must be considered, and the trapping potential must be modified accordingly. The fundamental scaling of potential energy and scattering rate discussed in the previous section will remain valid. We consider the dressed atom state picture in the presence of a laser field. Using second-order time-independent non-degenerate perturbation theory. The correction or shift in energy levels caused by a perturbing Hamiltonian \mathcal{H}_1 can be written down.

$$\Delta E_i = \sum_{j \neq i} \frac{|\langle j | \mathcal{H}_1 | i \rangle|^2}{\mathcal{E}_i - \mathcal{E}_j} \quad (2.26)$$

where \mathcal{E}_i is the energy of dressed level, for atom in laser light, the interaction Hamiltonian is $\mathcal{H}_i = -\hat{\mu}\mathbf{E}$ with $\hat{\mu} = -e\mathbf{r}$ is the electric dipole operator. When an atom in its ground state interacts with a field, it has zero internal energy while the field energy $n\hbar\omega$ is determined by the number of photons n and the energy of each photon $\hbar\omega$. For the unperturbed state, the total energy \mathcal{E}_i is equal to $n\hbar\omega$. However, if the atom is excited to a higher energy state by absorbing a photon, the internal energy is $\hbar\omega_0$ and the field energy is $(n-1)\hbar\omega$. Hence, the energy of the excited state is $\mathcal{E}_j = \hbar\omega_0 + (n-1)\hbar\omega = -\hbar\Delta_{ij} + n\hbar\omega$, where Δ_{ij} is the difference in energy between the two levels $\mathcal{E}_i - \mathcal{E}_j = \hbar\Delta_{ij}$. The energy level shift can be determined from:

$$\Delta E = \pm \frac{|\langle e | \mu | g \rangle|^2}{\Delta} |E|^2 = \pm \frac{3\pi c^2 \Gamma}{2\omega_0^3 \Delta} I \quad (2.27)$$

for the ground state, the energy shift is below the unperturbed state; for the excited state, the energy is shifted above the unperturbed state. Because the energy shift is a function of intensity, a laser beam with a Gaussian intensity distribution will result in a nearly harmonic trapping potential for the atoms in the ground state. For a multilevel situation, Eq. 2.27 can be generalized as :

$$\Delta E_i = \frac{3\pi c^2 \Gamma}{2\omega_0^3} I \sum_j \frac{c_{ij}^2}{\Delta_{ij}} \quad (2.28)$$

where the summation is over all possible electronically excited state $|e_j\rangle$. The calculation of the state-dependent ground-state dipole potential $U_{Dip,i} = \Delta \mathcal{E}_i$ requires consideration of all coupled excited states $|e_j\rangle$, taking into account their respective line strengths c_{ij}^2 and detuning Δ_{ij} .

2.4.3 Red-Detuned Dipole Traps

When the light field is tuned lower than the atomic transition frequency (red detuning), the dipole force points towards the increasing intensity. However, The weak trapping forces created by tightly focused lasers beam were the greatest barrier to capturing neutral atoms in the dipole trap. With a tightly focused beam, the attainable trap depths are usually in the milli-Kelvin range, which is several orders of magnitude smaller than the thermal energy of room-temperature atoms.

There are three distinct configurations for creating red-detuned dipole traps using Gaussian beams. These include *Focused Beam Traps*, which require a single tightly focused beam, *Standing-Wave Traps*, where atoms are axially trapped in the antinodes of the standing-wave created by retroreflecting the beam while conserving the curvature of the wave fronts and the polarization, and *Crossed-beam Traps*, created by two or more beams intersecting at their foci.

A Focused-Beam Trap

A far red-detuned focused Gaussian beam can create dipole potential, which can trap atoms in the maxima of intensity as shown in Fig. 2.3.

As discussed in the previous section dipole potential and scattering rate of the dipole trap depend on the intensity of the beam. For a Gaussian Beam with total power P, the spatial intensity distribution is given by:

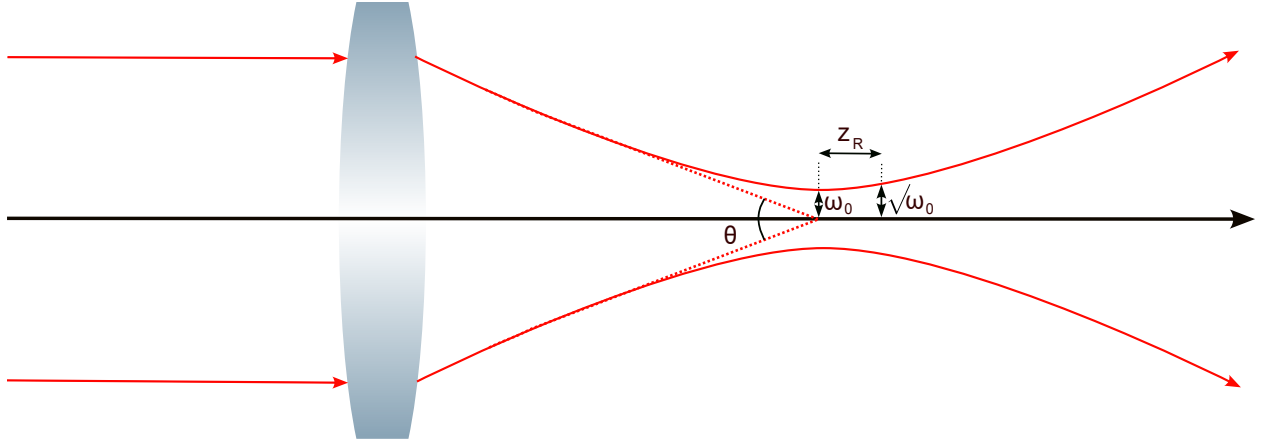


Figure 2.3: Focused Gaussian Beam

$$I(r, z) = \frac{2P}{\pi\omega^2(z)} \exp\left(-2\frac{r^2}{\omega^2(z)}\right) \quad (2.29)$$

for a beam propagating in z direction, r representing the radial coordinate, and $\omega(z)$ is the beam waist, defined as the distance from the centre in the radial direction, for which the intensity decreases to $1/e^2$ of the maximum value. The dependence of $\omega(z)$ on the axial coordinate z is:

$$\omega(z) = \omega_0 \sqrt{1 + \left(\frac{z}{z_R}\right)^2} \quad (2.30)$$

where ω_0 is the minimum radius of beamwaist and z_R denotes the Rayleigh Length given as:

$$z_R = \pi\omega_0^2/\lambda \quad (2.31)$$

The Dipole potential and Scattering rate for the trap created using a focused Gaussian beam can be calculated using Eqs. 2.29, 2.21 and 2.22.

In situations where the thermal energy of an atomic ensemble, denoted by $k_B T$, is much lower than the potential depth \hat{U} , the radial expansion of the atomic cloud is relatively small when compared to the beam waist, and the axial expansion is relatively small when

compared to the Rayleigh range. In such cases, the harmonic term in the Taylor expansion of the potential energy function around the minima is of interest and can be expressed as:

$$U(r, z) \simeq -\hat{U} \left[1 - 2 \left(\frac{r}{\omega_0} \right)^2 - \left(\frac{z}{z_R} \right)^2 \right] \quad (2.32)$$

As a result, the trapping frequency near the bottom of the trap in the Radial direction is given as:

$$\omega_r = \sqrt{\frac{4\hat{U}}{m\omega_0^2}} \quad (2.33)$$

and in the Axial direction, the trapping frequency is:

$$\omega_z = \sqrt{\frac{2\hat{U}}{mz_R^2}} \quad (2.34)$$

Eqs. 2.33 and 2.34 shows that the radial frequency is substantially higher than the axial frequency, resulting in greater confinement along the radial direction of the laser beam and less confinement along the axial direction, which is the direction of the propagation of the beam.

2.5 Cooling Methods

Atoms exiting the oven have velocities of the order of 100 m/s, and the most suitable method for trapping and cooling of these atoms is to utilise the radiation pressure traps explained in section 2.2. Doppler Cooling and Sub-Doppler Cooling are two of the most prevalent approaches based on this phenomenon of momentum transfer from the light beam to atoms.

2.5.1 Doppler Cooling

Atomic velocities in a classical ensemble of atoms follow the Maxwell-Boltzmann distribution. According to the energy equipartition theorem, the relationship between thermal energy and translation energy for an atom of mass m is given by:

$$\frac{3}{2}k_bT = \frac{1}{2}mv_{rms}^2 \quad (2.35)$$

where v_{rms} is the root-mean-square velocity at temperature T . For monoatomic gas v_{rms} is given by:

$$v_{rms} = \sqrt{\frac{3\pi}{8}\bar{v}} \quad (2.36)$$

Eqs. 2.35 and 2.36 show that in order to cool the cloud of atoms, we have to reduce the average velocity of the ensemble.

In the scenario where a low-intensity laser beam with a frequency ω_L , which is tuned slightly lower than the atomic resonance frequency ω_0 ($\omega_L < \omega_0$), interacts with a two-level atom moving against the direction of the laser beam at velocity \vec{v} , the atom experiences a Doppler shift in frequency. The frequency shift can be calculated using the following equation:

$$\omega = \omega_L - \vec{k}\vec{v} \quad (2.37)$$

which is higher than ω_L as $\vec{k}\vec{v} < 0$ for the given case. Hence for a red-detuned laser frequency, atoms will experience the resonance frequency if,

$$\omega_L \left(1 + \frac{v}{c}\right) = \omega_0 \quad (2.38)$$

when the laser frequency is on resonance, the photon is absorbed, and it causes the atom to slow down.

When an atom and the laser beam are co-propagating, the Doppler shift causes an increase in the detuning between the frequency of the laser beam and the resonance transition frequency of the atom. As a result, absorption probability will decrease. Hence, the atom will experience an unbalanced force due to the two laser beams depending upon the velocity \vec{v} . In the moving atom frame of reference, the force due to single photon absorption is given by Eq. 2.4. Force due to two weak counter-propagating beams can be calculated by adding the force due to individual beams.

$$F_{1D} = F_+ + F_- \quad (2.39)$$

and

$$\vec{F}_{+,-} = \pm \hbar \vec{k} \frac{\Gamma}{2} \frac{I/I_{Sat}}{1 + I/I_{Sat} + [2(\Delta \mp \omega_D)/\Gamma]^2} \quad (2.40)$$

where ω_D is the Doppler shift given as:

$$\omega_D = -\vec{k}\vec{v} \quad (2.41)$$

The force exerted on an atom from Eq. 2.40 dampens the movement of atoms for all velocities Fig. 2.4 show F_+ , F_- and F_{1D} forces acting on the atom. If the laser is tuned below an atomic resonance, the motion of atoms is dampened. Furthermore, there exists a small interval of velocities where the dependence of force on velocity is linear. For atoms with low velocity ($|\omega_D| \ll \Delta$), Eq. 2.40 can be simplified by neglecting second and higher order terms in ω_D .

$$F_{1D} \simeq -\beta \vec{v} \quad (2.42)$$

where β is the damping constant given by:

$$\beta = -8\hbar k^2 \frac{\Delta}{\Gamma} \frac{I/I_{Sat}}{[1 + I/I_{Sat} + (2\Delta/\Gamma)^2]^2} \quad (2.43)$$

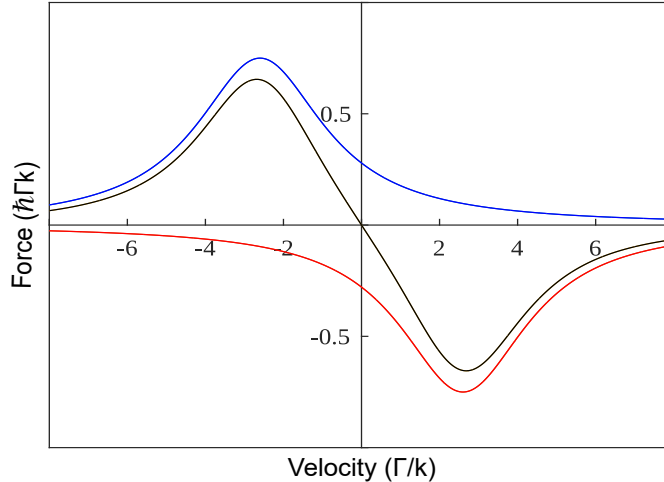


Figure 2.4: Damping force dependence on the velocity of atoms moving in 1D optical molasses. The blue curve shows the dependence of F_+ on velocity, the red curve shows the behaviour of F_- on velocity, and the black curve represents the total force on the atom moving in optical molasses.

Since the absorption and emission processes are stochastic in nature, the atom performs a random walk in momentum space, resulting in heating produced by momentum diffusion. When this heating rate and cooling rate become equal, it results in a lower limit of temperature that can be reached using Doppler cooling. This lowest possible temperature is referred to as the Doppler cooling limit. For low intensity ($I/I_{Sat} \ll 1$) and detuning $\Delta = -\Gamma/2$, lowest achievable temperature T_D or Doppler cooling limit is:

$$k_B T_D = \frac{\hbar\Gamma}{2} \quad (2.44)$$

In case of ^{87}Rb , the natural linewidth $\Gamma = 2\pi \times 6.1$ MHz and calculated Doppler limit is $T_D = 146 \mu K$.

For simplicity, we examined a 1D model in the previous decision. This model, however, can be extended to 2D and 3D systems by introducing pairs of additional counter-propagating beams from each dimension. In 1985, Steven Chu reported the first experimental demonstration of optical molasses [6].

2.5.2 Sub-Doppler Cooling

The precise temperature measurement of atoms in optical molasses in 1988 showed that the observed temperatures were significantly lower than the expected Doppler temperatures [19]. As a result, these experimental evidences of temperature measurements below the Doppler Cooling limit necessitated the development of a new theoretical model for the cooling mechanism that could explain the recorded sub-Doppler temperatures. The Doppler Cooling theory has limitations because two crucial properties were not taken into consideration in this theoretical model of optical molasses. First, the multiplicity of sublevels in the ground state of the atom and different light shifts for the corresponding sublevels. Second, the polarisation gradients produced by the interfering laser beams cause varying polarisation over an optical wavelength scale, resulting in a spatially dependent light shift of the ground sublevels. These gradients produce an effective potential for moving atoms. When the polarisation and multiplicity of the ground states of atoms are considered, it leads sub-Doppler cooling processes, described by a new theoretical model proposed by Dalibard and Cohen-Tannoudji [7].

There are two standard methods for achieving sub-Doppler cooling: The first method uses two counter-propagating waves with opposite circular polarisations ($\sigma^+ - \sigma^-$), creating standing waves with a rotating polarisation vector that maintains the same ellipticity. The second method uses two counter-propagating waves with orthogonal linear polarisations ($lin \perp lin$), resulting in laser polarisation with varying ellipticity in space but a fixed principal polarisation axis.

To understand the two configurations, we will consider a 1D model, where a multilevel atom interacts with two counter-propagating laser beams. For $\sigma^+ - \sigma^-$ configuration, if the intensity (amplitude) of the two beams are equal, it results in linear polarisation with polarisation vector rotating along the principle axis forming a helix with a pitch λ (wavelength of laser). In the $lin \perp lin$ configuration, the orientation of the principal axis of polarisation remains fixed, while the ellipticity of the polarisation changes along the direction of propagation. Specifically, the polarisation changes from linear at $z = 0$ to (σ^-) circular at $z = \lambda/8$, to linear at $z = \lambda/4$, to (σ^+) circular at $z = 3\lambda/8$, to linear at $z = \lambda/2$, and so on.

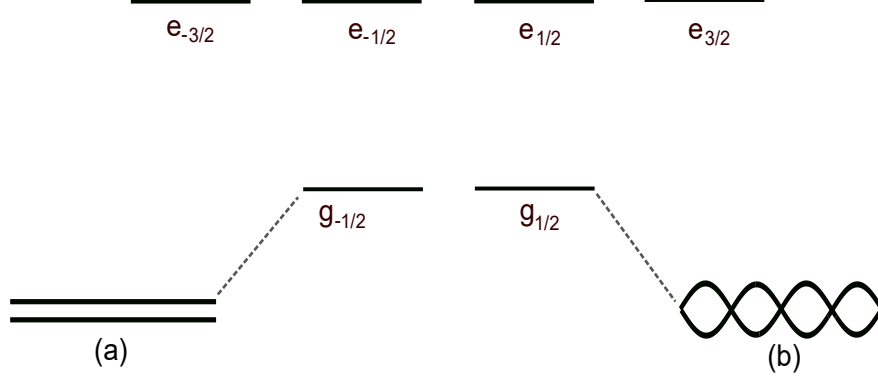


Figure 2.5: Light shift for ground state sublevel. (a) light shift due to $\sigma^+ - \sigma^-$ configuration. (b) light shift due to $lin \perp lin$ configuration.

A ($lin \perp lin$) Configuration.

In the $lin \perp lin$ configuration, the Clebsch-Gordan coefficients for various transitions $g_m \longleftrightarrow e_{m'}$ are different. Because the polarisation changes along the z direction, the two light-shifted energies oscillate with z . When the polarisation is linear, both sublevels are equally shifted. However, for an σ^+ polarisation, the $g_{1/2}$ sublevel is shifted the most, and for an σ^- polarisation, the $g_{-1/2}$ sublevel is shifted the most.

In order to understand the cooling process for the $lin \perp lin$ configuration, let us examine the transition between $J_g = 1/2$ and $J_e = 3/2$. Fig. 2.6 shows the Clebsch-Gordan coefficients for the different $g_m \longleftrightarrow e'_m$ transitions. The square of these coefficients represent the respective transition probabilities.

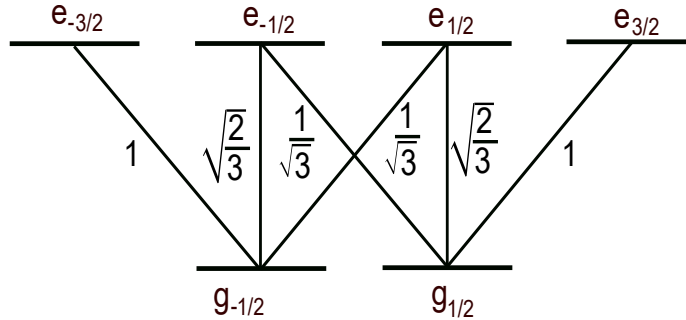


Figure 2.6: Clebsch-Gordan Coefficient for $J_{1/2} \longleftrightarrow J_{3/2}$ transition

Atom At Rest

In this particular model, the atom is stationary, and there are two counter-propagating beams that are red-detuned from the resonance frequency. The energy levels and populations of the two ground-state sublevels are dependent on the position along the z -axis. For an atom positioned at $z = \lambda/8$, the polarization is σ^- , and the atom is optically pumped in $g_{-1/2}$. As a result, the steady-state populations ground state sublevels $g_{-1/2}$ and $g_{1/2}$ are 1 and 0, respectively. Since the σ^- transition originating from $g_{-1/2}$ is three times stronger than the σ^+ transition originating from $g_{1/2}$, the light shift Δ_- of $g_{-1/2}$ is three times greater in magnitude than the light shift Δ_+ of $g_{1/2}$. Since the atom is in a red-detuned laser beam, the energy shift for both of the ground-state sublevels will be negative.

When the atom is positioned at $z = 3\lambda/8$, the polarisation is σ^+ , and the atom is optically pumped to the $g_{1/2}$ ground state sublevel. As a result, the steady-state populations for the $g_{-1/2}$ and $g_{1/2}$ ground-state sublevels are 0 and 1, respectively. The energy level shift will be negative as the laser beam is red-detuned, but now Δ_+ will be three times greater in magnitude than Δ_- .

If the atom is positioned at $z = 0, \lambda/4, \lambda/2, \dots$, the atom is in linear polarisation, therefore the light shift is still negative; however, the shift for the two ground state sublevels is equal in magnitude, and it is $2/3$ of the maximum shift found in the $\sigma^- - \sigma^+$ polarisation case discussed in following section. The Fig. 2.7 summarises the light shift in energy sublevels caused by polarization discussed in this model.

Moving Atom (Sisyphus Effect)

Suppose that the atom is moving along the z -axis. In this case, it takes a finite amount of time τ_P for optical pumping between the two ground-state sublevels. Assuming that the atom is initially located at the bottom of a potential valley, such as at $z = \lambda/8$, and moves to the right, if the atom's velocity v is such that it covers a distance of the order of $\lambda/4$ during τ_P , the atom will typically remain on the same sublevel, climb the potential hill, and reach the top of the hill before being optically pumped to the other sublevel, i.e., to the bottom of the next potential valley located at $z = 3\lambda/8$. This sequence can then be repeated.

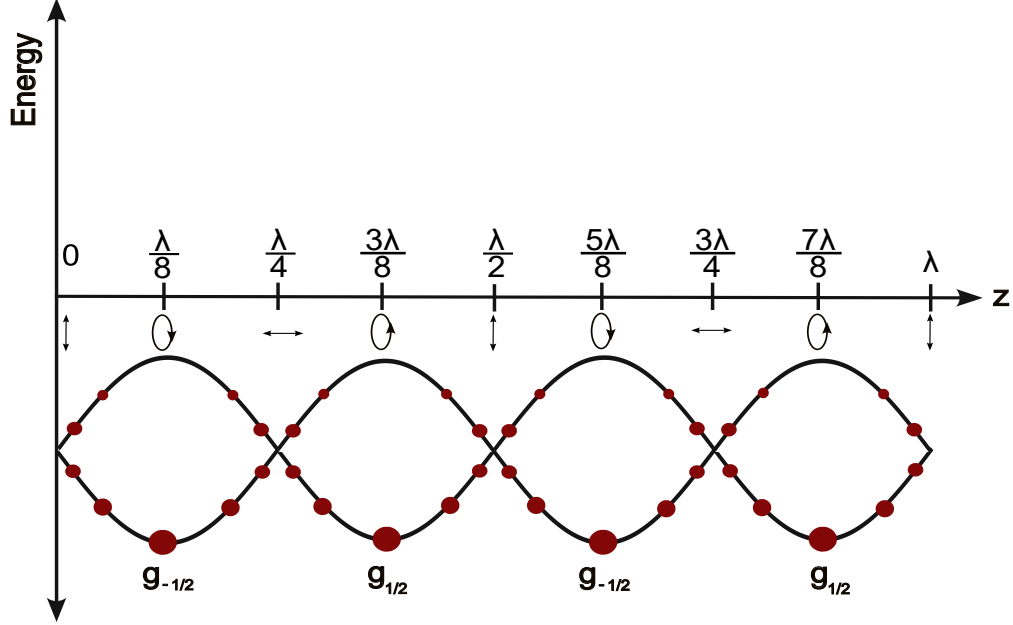


Figure 2.7: Light shifted (AC stark shift) energy levels and steady-state population for ground state $J_{1/2}$ in $lin \perp lin$ configuration.

Due to the time delay τ_P , the atom appears to be continuously climbing potential hills, converting some of its kinetic energy into potential energy. This is similar to the cooling effect seen in stimulated molasses and is an atomic illustration of the Sisyphus myth. Fig. 2.8 provides a brief summary of the atomic Sisyphus effect.

The energy dissipation mechanism for this cooling effect can be explained through momentum redistribution. The momentum of the laser field can change as a result of a redistribution of photons between two waves moving in opposite directions, which occurs through the process of stimulated emission. This process is reversible, with photons being absorbed from one wave and transferred to the other. However, optical pumping introduces irreversibility, which is necessary for energy dissipation and cooling. As illustrated in Fig. 2.8, as the atom travels along the z -axis and reaches the top of a potential hill, it is more likely to absorb a photon with energy $\hbar\omega_L$ and emit a fluorescence photon that is blue-shifted by the light shift splitting between the two ground-state sublevels. The excess energy is carried away by spontaneous Raman anti-Stokes photons, which dissipate the potential energy gain at the expense of kinetic energy.

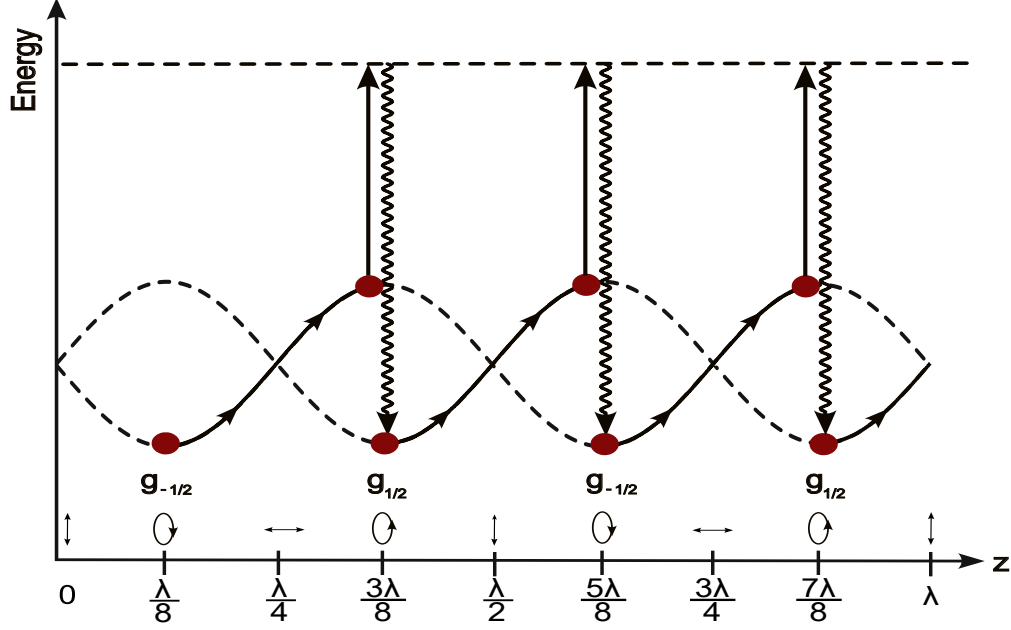


Figure 2.8: Sisyphus effect on an atom moving in $lin \perp lin$ configuration

B $(\sigma^+ - \sigma^-)$ Configuration.

In the $(\sigma^+ - \sigma^-)$ laser configuration, the polarization of the laser remains linear, but it rotates around the z -axis, creating a helix with an λ -pitch. This means that as the atom moves along the z -axis, the light shift of the ground-state sublevels does not change and there is no Sisyphus effect.

The cooling process for the $J_g = 1/2 \longleftrightarrow J_e = 3/2$ transition can be explained by the exchange of photons between the two counter-propagating waves. The atom absorbs a photon from one wave and releases it to the opposite wave via stimulated emission. However, due to the conservation of angular momentum, such an exchange is not possible in this configuration. When an atom absorbs an σ^+ photon, it is excited to either $e_{1/2}$ or $e_{3/2}$, but there are no transitions starting from these levels that can result in the stimulated emission of an σ^- photon.

$(\sigma^+ - \sigma^-)$ configuration introduces distinct cooling mechanics for atoms with $J_g \geq 1$. To explain this cooling phenomenon, we will use the simplest possible atomic transition, the $J_g = 1 \longleftrightarrow J_e = 2$ transition shown in Fig. 2.9

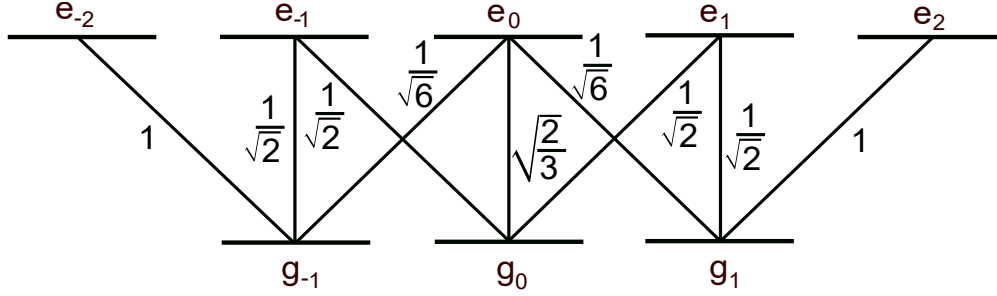


Figure 2.9: Clebsch-Gordan Coefficient for $J_1 \longleftrightarrow J_2$ transition

Atom at Rest

Let's assume that the atom is initially at rest at $z = 0$. We choose the quantization axis along the local polarization, which is along the y -axis at $z = 0$. Then, we have the eigenstates of J_y (J : angular momentum), denoted as $|g_{-1}\rangle_y$, $|g_0\rangle_y$, and $|g_1\rangle_y$. We can use optical pumping with a π polarization along the y -axis to concentrate the atoms in the $|g_0\rangle_y$ state since the rate of optical pumping from $|g_{-1}\rangle_y \rightarrow |g_0\rangle_y$, which is proportional to $(1/\sqrt{2})^2 (1/\sqrt{2})^2 = 1/4$, is greater than the rate from $|g_0\rangle_y \rightarrow |g_{-1}\rangle_y$, which is proportional to $(\sqrt{2/3})^2 (1/\sqrt{6})^2 = 1/9$. As a result, the steady-state populations of $|g_0\rangle_y$ and $|g_{\pm 1}\rangle_y$ are $9/17$ and $4/17$, respectively.

The π transition starting from $|g_0\rangle_y$ is $4/3$ time more stronger than π transition starting from $|g_{\pm 1}\rangle_y$, both these sublevels have equal light shift Δ_{\pm} which is $4/3$ time smaller in magnitude compared to the shift Δ_0 in $|g_0\rangle_y$. For a red-detuned light, the shifts Δ_{\pm} and Δ_0 will be negative, as shown in Fig. 2.10.

Moving Atom

As shown in Fig. 2.9, an atom in the $|g_{-1}\rangle$ state has a six-fold higher likelihood of absorbing a σ^- photon travelling towards $z < 0$ compared to a σ^+ photon moving towards $z > 0$. The opposite holds for an atom in the $|g_1\rangle$ state. If the atom moves towards $z > 0$ and the detuning Δ is negative (i.e., red-detuned), the sublevel $|g_{-1}\rangle$ becomes more populated than $|g_1\rangle$. This leads to unbalanced radiation forces exerted by the σ^- and σ^+ waves. The atom scatters more counter-propagating σ^- photons than co-propagating σ^+ photons, which dampens its velocity. This new cooling method works for significantly lower velocities than Doppler cooling for low intensity, where $|\Delta| \ll \Gamma$ and $kv/|\Delta|$ is substantially larger than the equivalent Doppler cooling parameter kv/Γ .

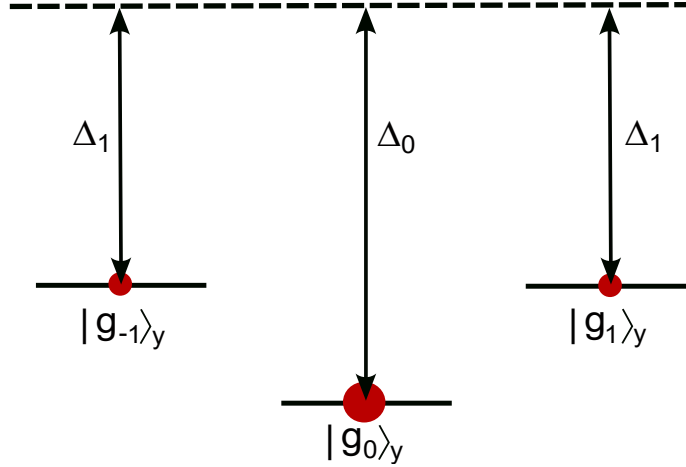


Figure 2.10: Light shifted ground state sublevels for $J_1 \longleftrightarrow J_2$ in $\sigma^+ - \sigma^-$ configuration. Steady State population of the sublevels are $4/17$, $9/17$, $4/17$ respectively, and $\Delta_0 = 4/3\Delta_1$

2.6 Magneto-Optical Trap (MOT)

In previous sections, we described how radiation pressure cools the thermal atoms coming from the oven. Magneto-Optical Trap (MOT) is the experimental realisation of the cooling methods discussed in section 2.5. In this section, we will go through the working principles of MOT.

Each atom travelling in two counter-propagating beams will be acted upon by a deceleration force many orders of magnitude greater than the accelerating force only when the atom is stationary both forces are balanced. This type of environment is known as optical molasses (OM). Atoms in OM are allowed to move around (via diffusion) inside the region of overlapping beams before gradually leaving it. The typical time scale for atom confinement in optical molasses is 100 ms. A spatially dependent restorative force is required to localise atoms in space. One way is to use an inhomogeneous quadrupole magnetic field generated by a pair of anti-Helmholtz. The magnetic field splits the Zeeman levels of the atoms, causing the transition frequency and radiative force to be position dependent. In addition to the dissipative cooling force, the magnetic field offers a restoring force with suitable laser beam polarisations. The Magneto-Optical Trap is a system that uses a magnetic field on optical molasses to cool atoms. There are several types of MOT arrangements, including Pyramidal MOT, Two-Dimensional MOT, and Three-Dimensional MOT. The most popular

configurations for laser cooling are 2D-MOT and 3D-MOT. Fig. 2.11 shows the 3D-MOT configuration.

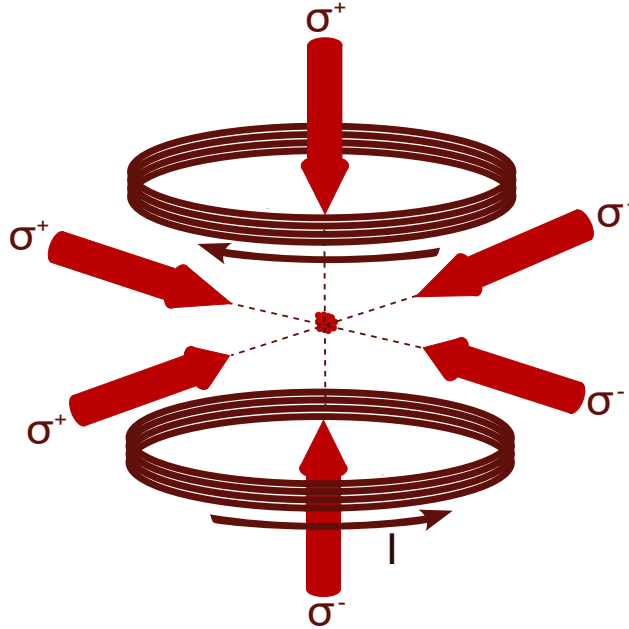


Figure 2.11: 3D-Magneto-Optical Trap. Arrows next to coils represent the direction of the current in the coils for respective polarisation configuration

The simplest case to understand MOT is to consider a 1D model. It consists of a σ^+ polarisation beam counter-propagating with σ^- polarisation beam along the z -axis, a pair of anti-Helmholtz coils to produce coaxial inhomogeneous quadrupole magnetic field \vec{B} , and an atom with hyperfine sub level $F = 0$ as the ground state and $F' = 1$ as the excited state. When a magnetic field is applied, the degeneracy of each hyperfine state F is lifted due to the Zeeman effect, resulting in $2F + 1$ sublevels. The sublevels are Zeeman shifted, which can be calculated by:

$$\Delta E_{m_F} = g_F \mu_B m_F B \quad (2.45)$$

where m_F is the magnetic quantum number and its value ranges from $m_F = -F, -F + 1, \dots, 0, \dots, F$, g_F is the Lande factor, μ_B is Bohr magneton and B is the magnetic field.

Consider an inhomogeneous magnetic field with a constant gradient $(\partial B / \partial z)$, in this region the sublevel splitting depends linearly on the distance from the trap centre, as shown in Fig. 2.12. At the centre of the trap, the magnetic field is zero since the two circular coils are

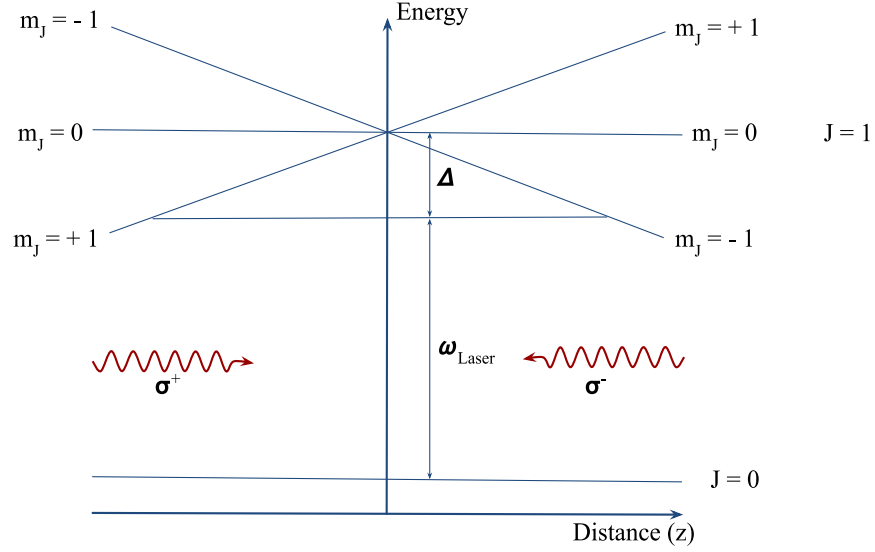


Figure 2.12: Zeeman Splitting of sublevel. The splitting of the sublevels is linear due to the constant magnetic field gradient.

in anti-Helmholtz configuration they cancel the effect of each other at the centre of the trap. For circular polarisation σ^+ , the absorption selection rule is $\Delta m = +1$, while for σ^- it is $\Delta m = -1$. Suppose the σ^+ polarised incident beam propagates towards the trap centre from the left, and the cooling conditions are satisfied, where transitions between sublevels $F = 0$ and $F' = 1$ are mainly driven by the σ^+ light. Momentum transfer takes place along the incident σ^+ beam towards the centre of the trap. At this location, the counter-propagating beam is significantly detuned from the resonance, resulting in minimal momentum transfer and negligible pushing of the atom out of the trap centre. Consequently, the atom is pushed towards the centre of the trap, where the magnetic field is zero. On the other hand, the σ^- polarised incident beam propagates towards the trap centre from the right. In this scenario, the σ^- beam is tuned much closer to the resonance compared to the σ^+ beam. This leads to momentum transfer in the direction of the σ^- beam, resulting in two forces acting on the atom. These forces always push the atom towards the trap centre, where they balance each other, resulting in a net force of zero on the atom.

In MOT, the total force on an atom is expressed as the sum of dissipative and restoring forces.

$$F_{MOT} = -\beta\vec{v} - \xi\vec{z} \quad (2.46)$$

The first term in the equation is the dissipative force given by Eq. 2.42, and the second term is the restoring force, where ξ is the dampening constant or spring constant given by:

$$\xi = \frac{\mu' \beta}{\hbar k} \frac{\partial B}{\partial z} \quad (2.47)$$

where μ' is the effective magnetic moment of the transition, given as:

$$\mu' = (g_e m_e - g_g m_g) \mu_B \quad (2.48)$$

where g_e and g_g are the Lande factors of the excited and the ground states, respectively, and m_e and m_g are the magnetic quantum number of the excited state and the ground state, respectively.

The above-mentioned 1D model can be expanded to 2D and 3D models with more sophisticated atomic hyperfine structures, and these systems are known as 2D-MOT and 3D-MOT systems, respectively.

2.7 Electromagnetically Induced Transparency

Electromagnetically induced transparency (EIT) is a phenomenon that occurs in an absorbing medium in presence of a coupling laser, resulting in reduced absorption at the line centre of the transition for a probe laser. EIT is based on coherent population trapping and can be classified into three types based on the configuration: Λ -type, V -type, and *Ladder*-type three-level system, each of the types is illustrated in Fig. 2.13.

In a Λ -type system, there are two ground states denoted by $|1\rangle$ and $|3\rangle$, and one excited state, denoted by $|2\rangle$. A coupling laser with Rabi frequency Ω is used to couple states $|3\rangle$ and $|2\rangle$, while a weak probe laser with Rabi frequency Ω_P is used to couple states $|1\rangle$ and $|2\rangle$. The excited state $|2\rangle$ has a decay rate given by Γ .

A V -type system consists of one ground state, $|2\rangle$, and two excited states, $|1\rangle$ and $|3\rangle$. A coupling laser with Rabi frequency of Ω couples states $|3\rangle$ and $|2\rangle$, while a weak probe laser

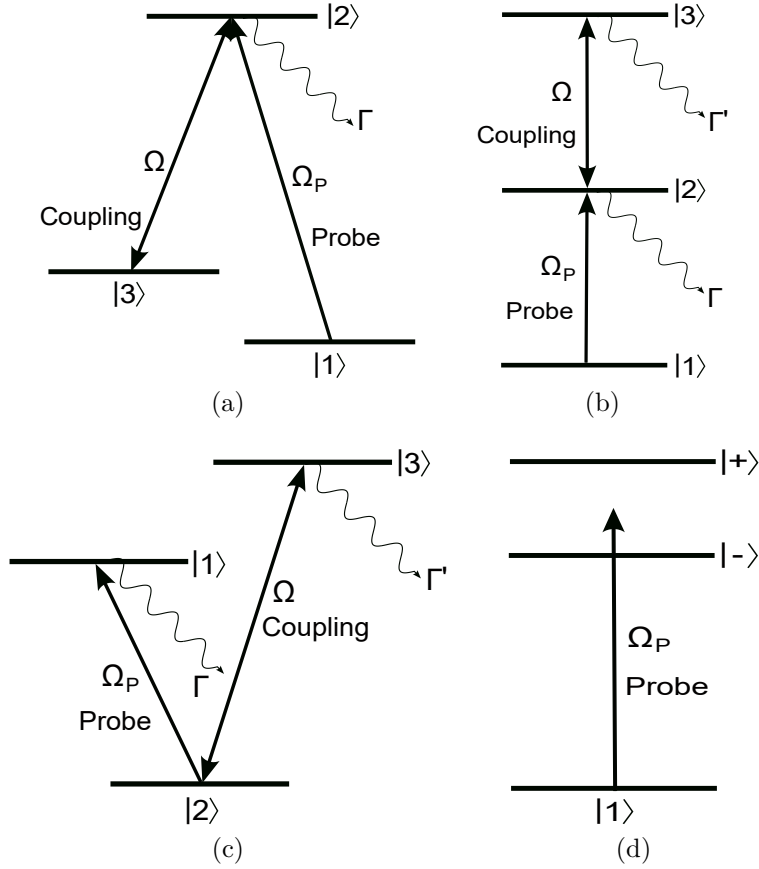


Figure 2.13: Λ -type three-level system (a). *Ladder*-type three-level system (b). *V*-type three-level system (c). Semi-classical dressed state picture of EIT (d)

with Rabi frequency of Ω_P couples states $|1\rangle$ and $|2\rangle$. The excited states $|1\rangle$ and $|3\rangle$ have spontaneous decay rates of Γ and Γ' respectively. Depending on the energy level difference between $|1\rangle$ and $|3\rangle$, $|3\rangle$ can be referred to as either the upper or lower excited state.

Ladder-type systems have a ground state $|1\rangle$, a excited state $|2\rangle$ and a higher excited state $|3\rangle$. A coupling laser with Rabi frequency Ω couples states $|3\rangle$ and $|2\rangle$, and a weak probe laser with Rabi frequency Ω_P couples states $|1\rangle$ and $|2\rangle$. The excited state $|2\rangle$ and higher excited state $|3\rangle$ have spontaneous decay rates Γ and Γ' , respectively.

EIT is defined as a decrease in the absorption of probe laser due to coupling laser; hence it is important to under the dynamics of atoms in the presence of probe laser [30]. As probe laser couples states $|1\rangle$ and $|2\rangle$, the response can be understood by density matrix element ρ_{12} . The probe absorption is represented by $Im(\rho_{12})$, and dissipative properties is represented

through $Re(\rho_{12})$. Considering, $\Gamma_{13} = 0$, where Γ_{13} is the decay rate of two-photon coherence between $|1\rangle$ and $|3\rangle$ and given by ρ_{13} element of density matrix, for a Λ -type system, density matrix element ρ_{12} is:

$$\rho_{12} = 0 \quad (2.49)$$

for a *Ladder*-type system, this density matrix is given by:

$$\rho_{12} = -\frac{i\Omega_P}{\Gamma + 2\Omega_P^2/\Gamma + \Omega^2/\Gamma'} \quad (2.50)$$

The Λ -type system shows complete transparency regardless of the intensity of the coupling laser. On the other hand, a *V*-type or *Ladder*-type three-level system always absorbs the probe field, and any reduction in absorption is due to the AC Stark effect of the coupling laser. Therefore, only the Λ -type system can be regarded as a true EIT system in this context.

Semi-Classical dressed state model in Fig. 2.13 can be used to understand these systems further, in this model $\Omega \ll \Gamma$ and Γ' . The coupling laser creates two dressed states $|+\rangle$ and $|-\rangle$, which are the superposition of the original states.

In the case of a Λ -type system, the two dressed states are:

$$|+\rangle = \frac{1}{\sqrt{2}} (|2\rangle + |3\rangle) \quad (2.51a)$$

$$|-\rangle = \frac{1}{\sqrt{2}} (|2\rangle - |3\rangle) \quad (2.51b)$$

In the case of a *Ladder*-type system, the two dressed states are given by:

$$|+\rangle = \frac{1}{\sqrt{2}} (|3\rangle + |2\rangle) \quad (2.52a)$$

$$|-\rangle = \frac{1}{\sqrt{2}} (|3\rangle - |2\rangle) \quad (2.52b)$$

The probe laser contains two excitation transitions that interfere with each other,

$|1\rangle \rightarrow |+\rangle$ and $|1\rangle \rightarrow |-\rangle$. The interference in the Λ -type system is destructive and completely inhibits probe absorption at the line centre.

The amplitude of excitation for a Λ -type system is:

$$P \propto \left| \frac{\langle 1|d \cdot E_p|+\rangle}{\Omega} + \frac{\langle 1|d \cdot E_p|-\rangle}{-\Omega} \right|^2 = 0 \quad (2.53)$$

The interference in the *ladder*-type system is constructive, and the probe absorption is enhanced near the line centre with the amplitude given by:

$$P \propto \left| \frac{\langle 1|d \cdot E_p|+\rangle}{\Omega} + \frac{\langle 1|d \cdot E_p|-\rangle}{-\Omega} \right|^2 = \frac{\Omega_P^2}{\Omega^2} \quad (2.54)$$

The decay rate of Γ_{13} , the two-photon coherence given by density matrix element ρ_{13} , can also be used to study the difference between the two systems. $\Gamma_{13} = 0$ for the Λ -type system and $\Gamma_{13} = \Gamma/2$ for the ladder-type system. Hence, the Λ -type system is the only configuration that can show complete EIT, defined as 100% EIT depth at the line centre. In contrast, the *Ladder*-type and *V*-type systems cannot exhibit complete EIT.

In a previous explanation, we explained the mechanism behind EIT using the AC Stark effect, which results in reduced absorption towards the line centre in all three types of systems. However, when the coupling field is weak to moderate, quantum interference plays a significant role and differs significantly between the Λ -type and the other two systems (*V*-type and *Ladder*-type): while the Λ -type system experiences destructive interference, the other systems experience constructive interference.

Transitions between degenerate magnetic sublevels must be considered while studying EIT because of the complex hyperfine structures of alkaline atoms. A laser-coupling method can form an Λ -type system by driving one of the ground hyperfine states, F_C , to one of the excited hyperfine levels, F' , while a probe laser couples a separate hyperfine ground state, F_P , to the same excited hyperfine state, F' . Complete EIT in the Λ -type system requires the magnetic sublevels of the F' excited state, which are coupled to the magnetic sublevels of the F_P state by the probe laser, also be coupled to the magnetic sublevels of the F_C state by the coupling laser. In other words, complete EIT demands that the sublevel m'_F of the hyperfine excited state F' be coupled to a magnetic sublevel m_{F_C} of the ground hyperfine state F_C by the coupling field among all possible probe transitions for a particular

polarisation configuration $m_{F_P} \rightarrow m'_{F'}$. The probe transition that satisfies this condition is referred to as a dark transition, as opposed to a non-dark transition. For Λ -type systems with a single coupling-laser beam, two sets of transitions fulfil this need for the complete EIT: first, $F_C = F'$ and $F_P = F' - 1$; second, $F_C = F' + 1$ and $F_P = F'$ or $F' - 1$.

Because of the absorption enhancement caused by constructive quantum interference, a three-level *ladder*-type system does not show complete transparency at the line centre. When the probe laser couples the ground hyperfine state F_P to the intermediate excited hyperfine state F' and the coupling laser couples the intermediate excited state F' to the higher excited state F'' , an alkali atom forms a *Ladder*-type system. When the same analysis is applied to the *Ladder*-type system, the highest absorption reduction or ideal transparency is achieved under either of the two identical conditions: first, $F_C + F'' = F'$ and $F_P = F' - 1$, or second, $F_C + F'' = F' + 1$ and $F_P = F'$ or $F' - 1$. We have used a *Ladder*-type system for the experiments described in this thesis.

Complete EIT of Λ -type system can also be understood from the Schrodinger equation. To construct the Hamiltonian for a two-level atom interacting with a single-mode field, we can write the detunings of a single photon as Δ_P and Δ_C , and the detuning of two photons as $\Delta = \Delta_P - \Delta_C$. This allows us to express the Hamiltonian in the appropriate rotating frame.

$$\hat{H} = -\Delta_P |3\rangle \langle 3| - \Delta |2\rangle \langle 2| - (\Omega_P |3\rangle \langle 1| + \Omega_C |3\rangle \langle 2| + \Omega_P^* |1\rangle \langle 3| + \Omega_C^* |2\rangle \langle 3|) \quad (2.55)$$

For simplicity, we can ignore the spontaneous decay term. And the eigenstate for the Hamiltonian is given as:

$$|\Psi\rangle = c_1(t) |1\rangle + c_2(t) |2\rangle + c_3(t) |3\rangle \quad (2.56)$$

In case, where the detuning of the two photons are equal i.e., $\Delta_P \sim \Delta_C = \Delta$, and Δ is large, the probability amplitude is given by:

$$c_3 = -\frac{\Omega_P c_1 + \Omega_C c_2}{\Delta} \quad (2.57)$$

Through the absorption of a photon on transition ν_P and subsequent emission of a photon with frequency ν_C , there is a coherent transfer of population between the two ground states, which results in a large coherence $\rho_{21} = c_2 c_1^*$. Despite neglecting the upper state decay, the excited state population is significantly reduced by the large detuning Δ , leading to a low probability for spontaneous emission.

For *Ladder*-type and *V*-type three-level systems, a similar equation can be derived. The main difference in the *Ladder*-type system are:

- There are dipole-allowed spontaneous emissions from the final state $|3\rangle$, as transitions to the intermediate state $|2\rangle$ are also dipole-allowed transition. Consequently, the two-photon resonances usually have a wider width. However, there is one significant exception to this trend, which is observed in the atomic Hydrogen $1s \rightarrow 2p \rightarrow 2s$ transition. In this case, the final state $2s$ is metastable and the fields used for two-photon resonance are far detuned from the $2p$ state.
- The properties of Doppler shift are unique for *Ladder*-type system due to the two-photon Raman transition absorption process as opposed to the Λ -type system, where one-photon absorption is followed by emission. As a result, the Doppler shifts will cancel the effect of the counter-propagating beams used in such system. This is because the different-frequency photons impart momentum kicks in opposite directions to the atom.

2.8 Rubidium Atoms

Rubidium is an alkali metal with the symbol Rb in the periodic table, an atomic number of 37, and an atomic mass of 85.4678 amu. It is a composite Boson because it has an even number of total fermions (electrons and nucleons). Nuclear spin has a half-integer value. Rubidium, like the other alkali group elements, is highly reactive in nature and rapidly oxidises in the air. Rubidium is a soft solid with a density of $1.53 \times 10^3 \text{ Kg/m}^3$ and a vapour pressure of $3.92 \times 10^{-7} \text{ Torr}$ at 25°C . The stable isotopes of rubidium are ^{85}Rb and ^{87}Rb , which have natural abundances of 72.17(2) % and 27.83(2) %, respectively. Strong electric dipole transitions in alkali metals facilitate laser cooling and trapping of alkali metals. *D1*

and D_2 transitions of alkali atoms are used as closed-cycle transitions for laser cooling. In the experiments, we have used ^{87}Rb .

^{87}Rb has 50 neutrons, 37 protons with nuclear spin of $3/2$, and 37 electrons arranged with electronic configuration $1s^2; 2s^2; 2p^6; 3s^6; 3d^{10}; 4s^2; 4p^6; 5s^1$. Fig. 2.14 show the ^{87}Rb D_2 transition hyperfine structure [29].

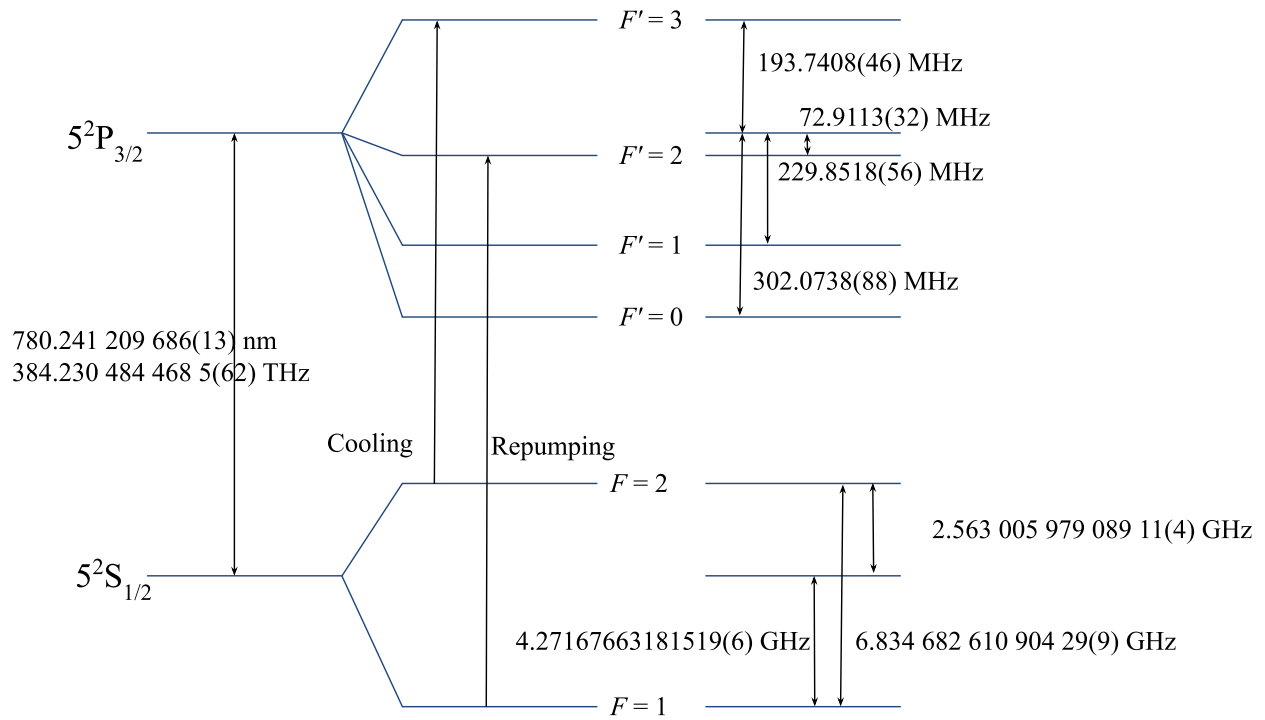


Figure 2.14: D_2 transition hyperfine structure of ^{87}Rb . Ground state values are taken from [4] and excited state values are taken from [3]

Experimental Setup

The laser cooling techniques outlined in the preceding chapter require a laser with a narrow linewidth. With the development of narrow-band tunable lasers in the 1970s. The laser linewidth is narrower than the natural linewidth, which led to the demonstration of several laser cooling techniques after the 1970s. This chapter describes the experimental setup based on the techniques presented in the preceding chapter.

3.1 Laser Frequency Stabilization

Current laser systems can generate beams with narrower linewidth than natural linewidth. However, the frequency of these lasers drifts from the central frequency owing to various factors, and certain experiments require linewidth even narrower than the default linewidth. All of the additional laser tunings need frequency stabilisation and linewidth reduction. There are several approaches for laser frequency stabilisation, but they all rely on error signal generation, which is detailed in this section.

An error signal is an electrical signal used in a feedback loop. An error signal requires a set point, which is the desired point at which the system should function, and system variables, which are monitored and regulated to bring the system to the set variable. The error signal indicates how far the system has progressed from the set variable to the feedback loop, as illustrated in Fig. 3.1. The error signal is given by:

$$\text{Error Signal} = \text{Set Point} - \text{System Variable}$$

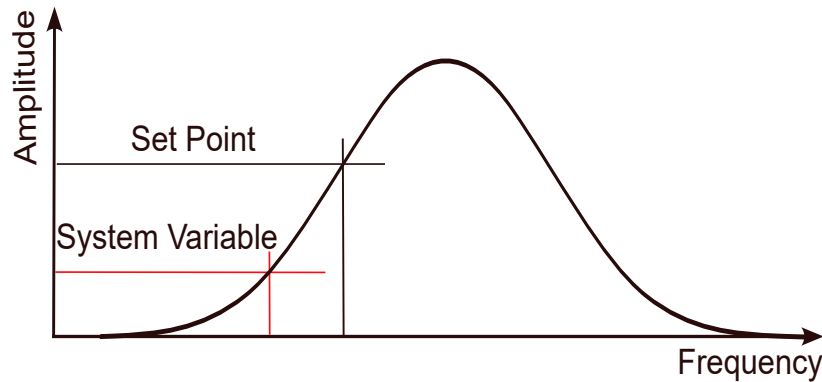


Figure 3.1: Resonance curve of an oscillator representing the desired point (set point) on the curve and the current position of the oscillator (system variable).

For active laser frequency stabilization, there are two main configurations: side fringe locking and top fringe locking.

3.1.1 Side-of-Fringe Locking

Fig. 3.2 illustrates the standard resonance curve used in locking. Side-of-Fringe locking is used to lock the system at a position that is neither the resonance's maxima nor minima but rather at another point on the resonance curve. Thus the term Side-of-Fringe locking. In Side-of-Fringe locking, an offset is added to the resonance curve so that the set point is on the x-axis, i.e. the y-coordinate of the set point is 0, as shown in Fig. 3.2. Now, if the system variable has a negative y-coordinate, it means that the system variable is on the left of the set point on the x-axis. The feedback loop must tune the variable so that it moves to the right towards the set point. If the system variable has a positive y-coordinate, it means that the system variable's x-coordinate is on the right of the set point, and the parameter must be tuned so that it moves to the right towards the set point. Locking at each point on the resonance curve can be explained using a similar analogy.

The main disadvantage of this type of locking is that fluctuations in the intensity of the laser change the set point of the system. As a result, another feedback loop is required to lock (stabilise) the intensity of the laser in order to keep the set point steady. The advantage

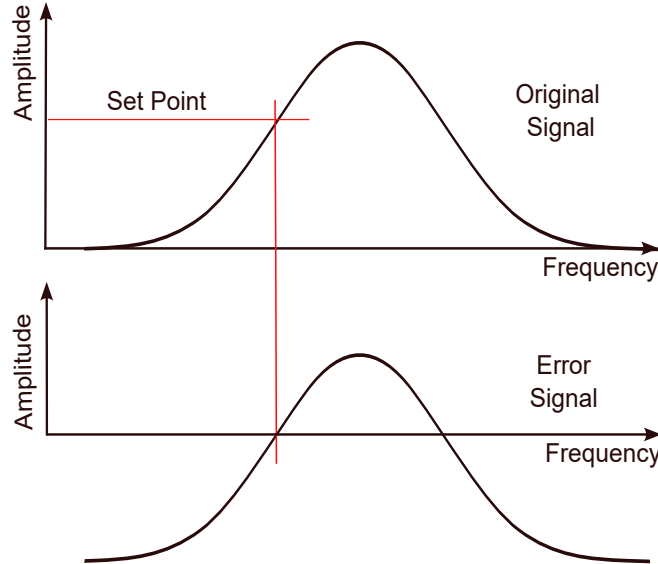


Figure 3.2: *Side-of-Fringe locking*: Resonance curve of an oscillator also referred to as Original Signal (*above*). Offset added to the original signal to make the value of the amplitude coordinate zero is called the Error signal (*below*)

of this configuration is that it can also lock the laser at frequencies that are not the maxima or the minima points of the resonance curve.

3.1.2 Top-of-Fringe Locking

Top-of-Fringe Locking is a technique for locking at the set point, at the resonance's local or global extremum. The Fig. 3.3 illustration shows top-of-fringe locking. This process requires modulating the laser frequency, recording the effect of modulation on the resonance curve with a photo-diode, and then demodulating the signal to produce the error signal. By modulating the frequency, we rapidly change the frequency around each point on the curve, and the effect is transferred to the amplitude of the curve, which is recorded using a photo-diode. The amplitude modulation due to frequency modulation is identical to the frequency modulation of the laser at the extremum; however, for points that are not at the extremum, the phase and amplitude of amplitude modulation due to frequency modulation depend on the slope and position of the corresponding point on the curve. After demodulating the photodiode signal, we obtain the error signal, which is the derivative of the resonance curve function. And this derivative curve can be used to determine if the system variable is to the right or the left of the set point, and variables are tuned accordingly to move the system

variable point towards the set point.

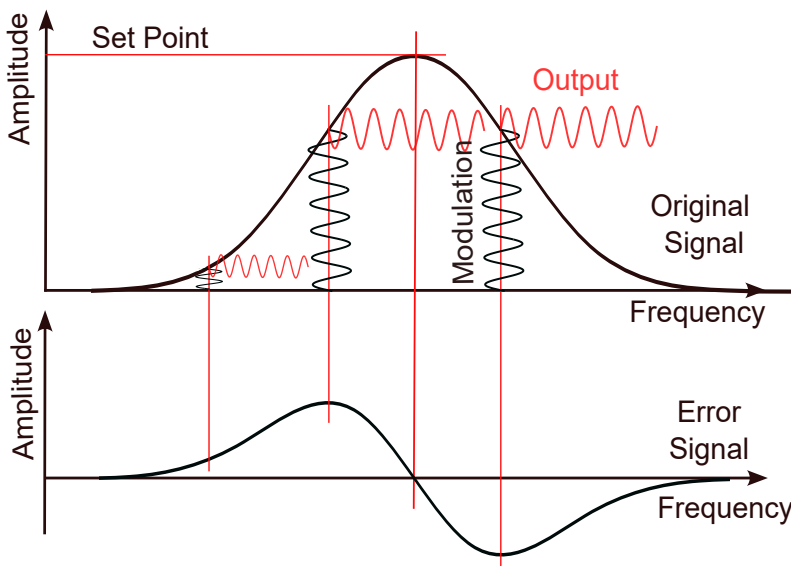


Figure 3.3: *Top-of-Fringe locking*: Resonance curve with frequency modulation (*above*). First Harmonics of after demodulation of output signal (*below*).

The advantage of this configuration is that fluctuations in laser intensity have no effect on the set point. Nevertheless, because the derivative at the extremum points is zero, this setup is used to lock at frequency points at the extremum of the resonance curve.

3.1.3 Saturation Absorption Spectroscopy

To generate an error signal, a reference is required. There are several ways to get a reference; two of the most commonly used reference systems are Fabry-Perot Cavity (PDH Locking) and Atomic Transition frequency. For all of the experiments, we used the atomic transition as a reference. Saturation Absorption Spectroscopy (SAS) of the atomic gas is done to use atomic transition as a reference.

Saturation spectroscopy is an incoherent nonlinear multi-photon interaction. It offers a simple way of determining the natural linewidth of an inhomogeneously broadened medium. Saturation spectroscopy is carried out using two counter-propagating beams, a probe beam and a pump beam, that have the same frequency ν and are close to resonance with the atomic transition frequency Δ . These two beams interact with different velocity classes due to Doppler shifts in the thermal atoms. The strong field (pump beam) interacts with atoms

that fulfil $\nu = \Delta + kv$, saturating their transition, whereas the weak field (probe beam) interacts with atoms that have been Doppler shifted by $\nu = \Delta - kv$. Both fields interact with stationary atoms during resonance. The two fields do not interact with the same group of atoms for the same detunings. When the frequency approaches the atomic resonance, $v \rightarrow 0$ and the two velocity classes begin to converge. Both fields interact with stationary atoms at resonance. As a result, the probe beam absorption spectra will have strong features around $\nu = \Delta$ due to stationary atoms saturated by the pump beam.

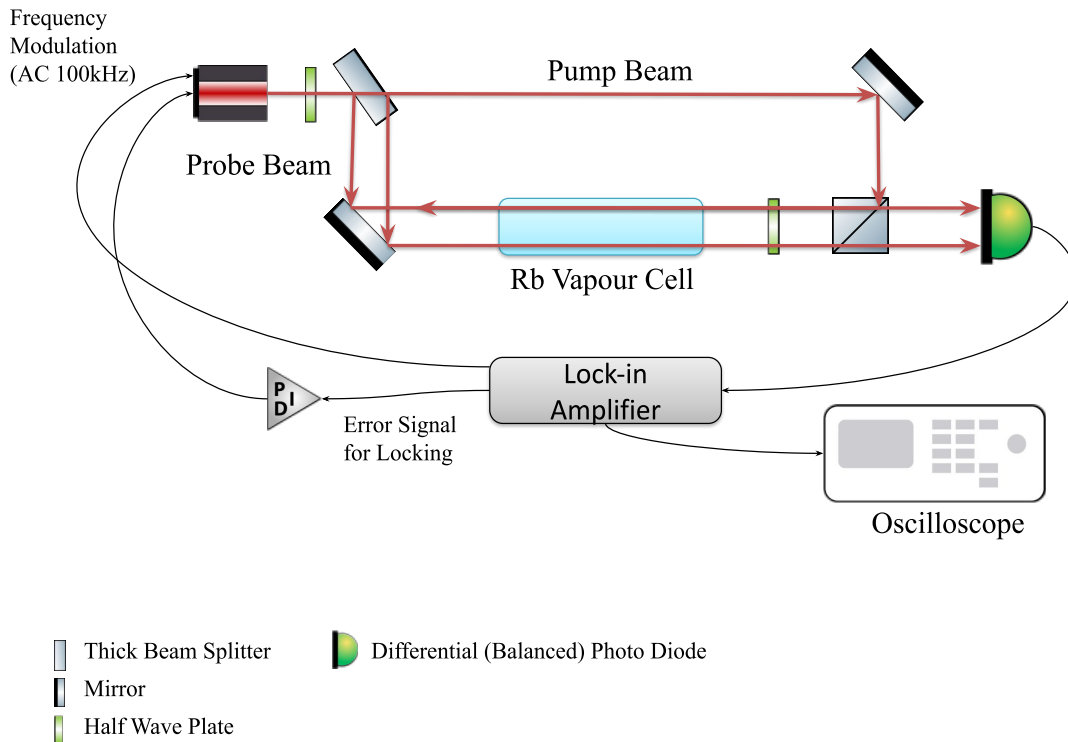


Figure 3.4: Experimental Setup for frequency stabilisation of laser using atomic transition as reference.

In the setup shown in Fig. 3.4, the laser beam is split using a thick beamsplitter, which divides the beam into three beams, one transmitted beam that serves as the pump beam and two reflected beams, one of which serves as the probe beam and the other as the reference beam to a balanced photodiode to remove the DC offset and other noises from the data recorded on the photo-diode. Modulation to the laser head is given from the Lock-in Amplifier as a 100 kHz sine wave into the AC Modulation port of the laser head. The signal from the balanced photodiode is demodulated using the same Lock-in Amplifier to generate

the error signal. This error signal is then sent into PID, which steers the system variables to the set point. Fig. 3.5 shows the transition used as a locking reference.

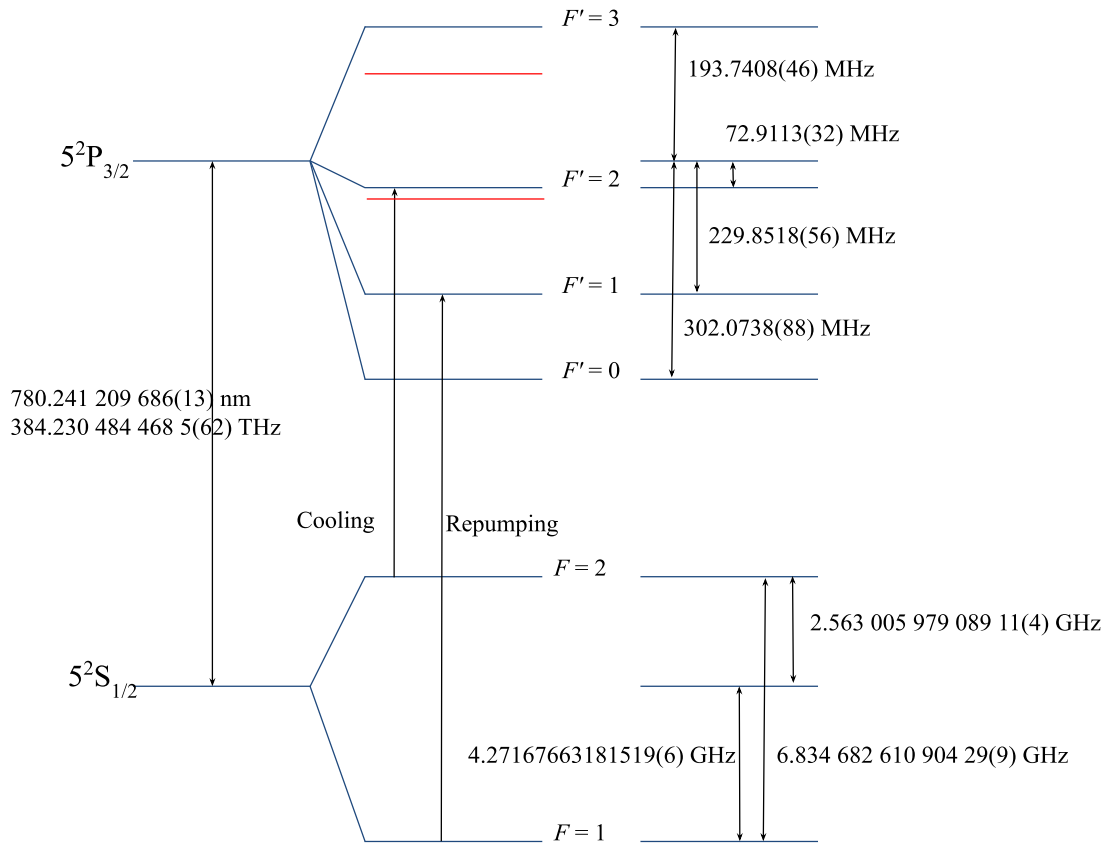


Figure 3.5: Transition used for frequency stabilisation of cooling and repumping lasers.

3.2 Two-Dimensional Magneto-Optical Trap

Two-Dimensional Magneto-Optical Trap (2D-MOT) is a popular way of cooling, particularly for Rubidium, since it provides low divergence and high efficiency owing to the large number of atoms in MOT loading with minimum laser power and robustness when compared to other methods of cooling.

A 2D-MOT system uses two pairs of counter-propagating beams that cross each other in the same plane to form Optical Molasses. These beams can cross one other at an angle of 90° or at an angle of 120° depending on the application, thus the term two-dimensional

magneto-optical trap. And two pairs of anti-Helmholtz coils for inhomogeneous quadrupolar magnetic field and optical molasses, as shown in Fig. 3.6.

The Experimental Setup of 2D-MOT consists of Vacuum Assembly, Magnetic Coils and Optical Arrangement. Fig. 3.6 Show the experimental setup of a 2D-MOT.

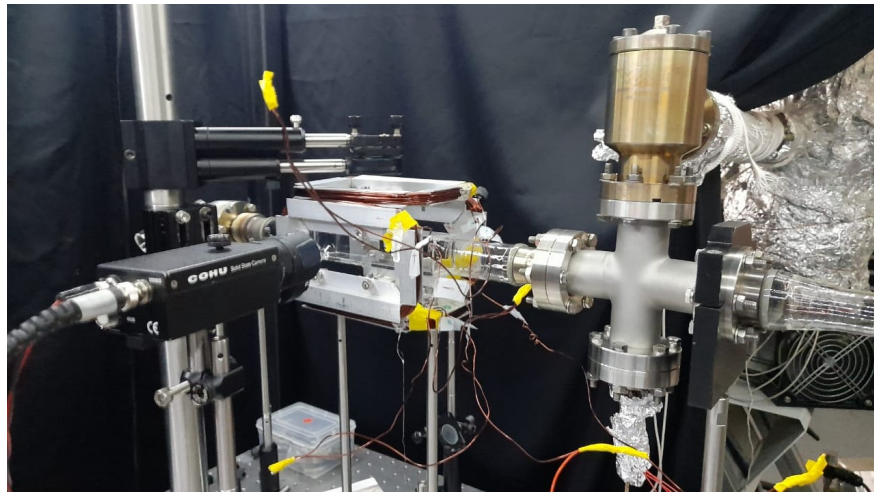
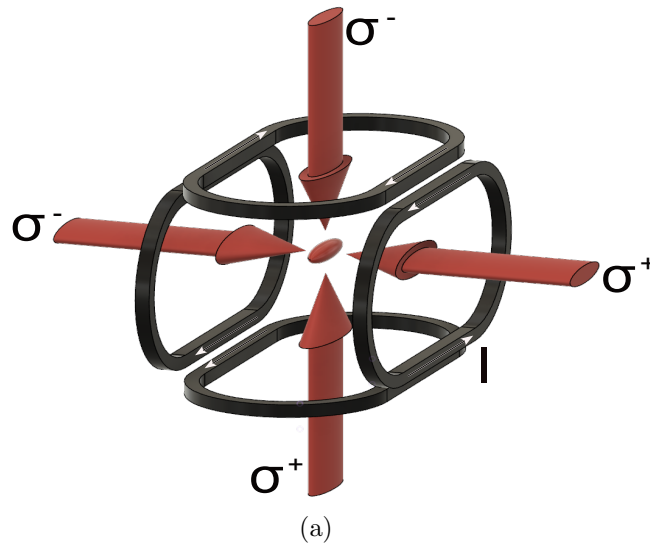


Figure 3.6: 2D-MOT Experimental setup. (a) schematic of a 2D-MOT, two pairs of anti-Helmholtz coils, the arrows on the coils representing the direction of current for the respective polarisation configuration. (b) Complete experimental setup of 2D-MOT with an IR camera for fluorescence imaging of cloud of cold atoms

The Vacuum Assembly consists of the main science chamber for MOT loading, a quartz cell with dimensions of $40 \times 40 \times 140$ mm with the inside pressure of 10^{-9} Torr. To demonstrate the push beam, one end of the quartz cell was attached to another quartz cell, while the other end was connected to a four-way cross nipple. The four-way cross nipple was attached to the Rubidium oven, which served as a source of thermal atoms. The opposite end was connected to the turbo molecular pump via an angel valve to close the vacuum assembly once the required pressure was attained. The end opposite to science chamber was closed with a viewport from the alignment of the push beam.

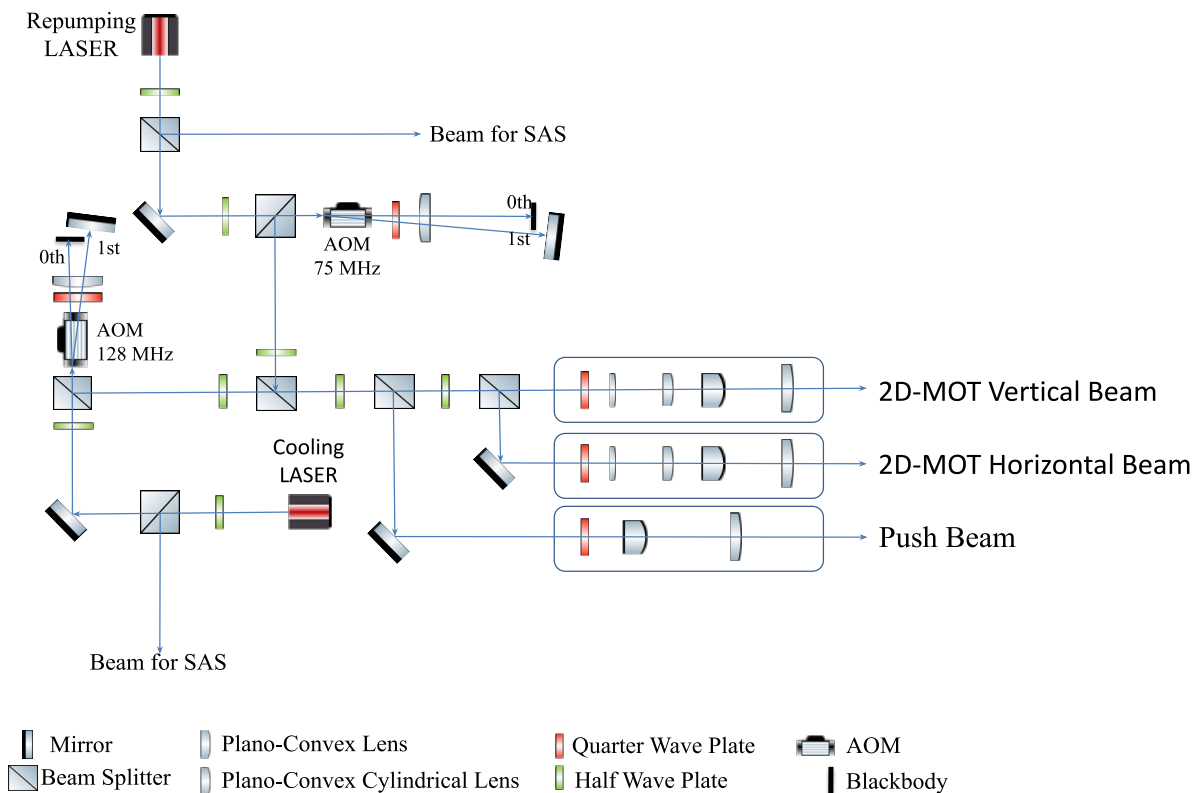


Figure 3.7: *Optical Bench layout.* Schematic arrangement of various optical components used to shape the laser beam for 2D-MOT.

For Optical Molasses, we have used a Toptica TA pro system as the cooling laser and a Toptica DL pro system as the repumping laser, both locked to the transitions shown in Fig. 3.5 using the technique outlined in section 3.1. The laser beam from the Cooling laser is first passed through an Acousto Optic Modulator (AOM) operating at 128 MHz in a double pass configuration which drives the frequency from the locked transition $F = 2 \rightarrow F' = 2$

frequency to the cooling transition $F = 2 \rightarrow F' = 3$ frequency with red-detuning of 10.650 MHz after which the beams are split into two, and passed through two cylindrical plano-convex lenses in telescope configuration to reshape the circular beam to elliptical beam and then aligned to form the optical molasses. The Toptica DL pro (repumping laser) was locked to a transition frequency of $F = 1 \rightarrow F' = 1$ transition and then passed through an AOM operating at 75 MHz in double pass configuration, shifting the frequency of the laser to a near resonance frequency of $F = 1 \rightarrow F' = 2$ transition with a red-detuning of 6.947 MHz and aligned to co-propagate with one of the cooling beams. The optical bench arrangement for 2D-MOT is shown in Fig. 3.7.

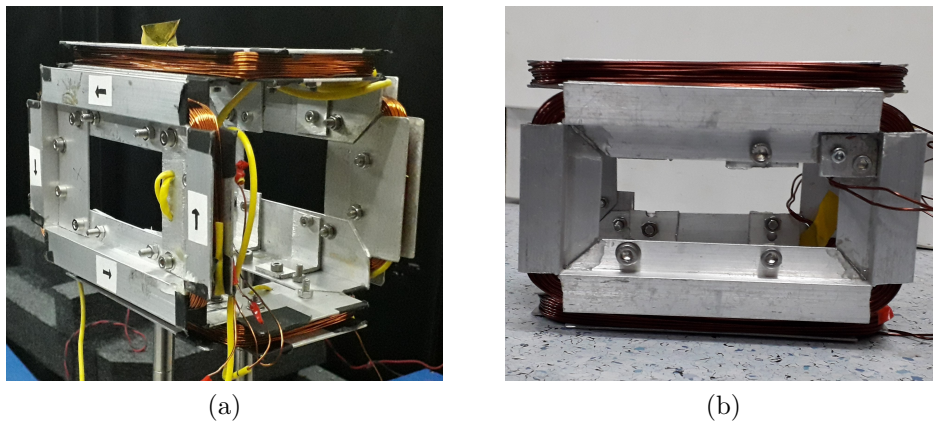


Figure 3.8: Magnetic Coils of 2D-MOT experimental setup.

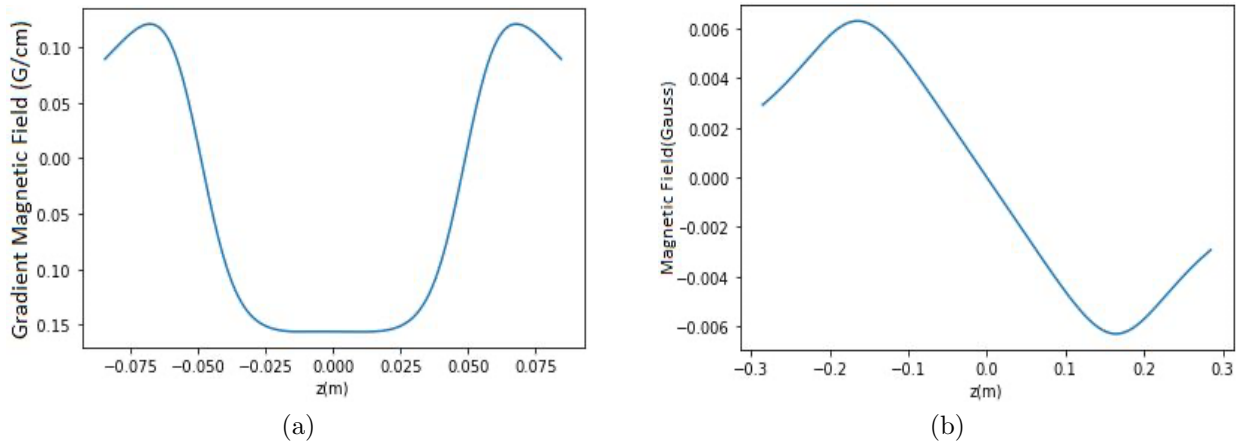


Figure 3.9: Magnetic field gradient profile (a). Magnetic field profile (b) of the magnetic field generated by magnetic coils shown in Fig. 3.8

Following Optical Molasses, two pairs of rectangular coils with dimensions of 70×140 mm with ten layers and seven turns in each layer were used to produce an inhomogeneous quadrupolar magnetic field as shown in Fig. 3.8. Each coil was operated at 4 A of current, resulting in a constant magnetic field gradient of 15 G/cm in a 2.5 cm long region at the structure's centre shown in Fig. 3.9. We detected the first indication of the cooling of thermal atoms and the formation of a cloud of cold atoms by aligning the magnetic field centre with optical molasses.

3.3 Three-Dimensional Magneto-Optical Trap

Three-Dimensional Magneto-Optical Trap (3D-MOT) is often used as the second stage of cooling in most setups, with Zeeman slower or 2D-MOT serving as the first stage of cooling. A 3D-MOT system, as shown in Fig. 3.10, uses a pair of counter-propagating beams from each of the three axes to produce the optical molasses and a pair of circular coils in anti-Helmholtz configuration to produce the required magnetic field.

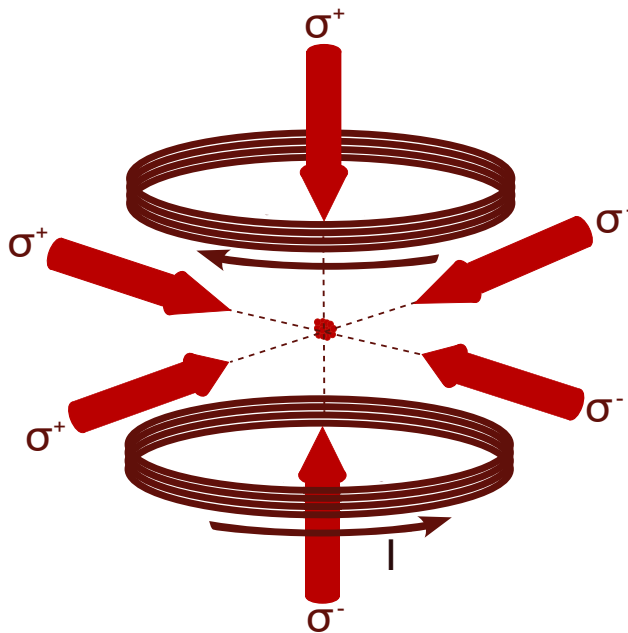


Figure 3.10: 3D-Magneto-Optical Trap. Arrows next to coils represent the direction of the current in the coils for respective polarisation configuration

Since the atoms in 3D-MOT are confined in all three dimensions, the cloud of atoms can be cooled to temperatures lower than those in 2D-MOT and Zeeman slower.

The principal part of the setup is Vacuum Assembly, around which the whole setup is designed. The science chamber is an octagon-shaped stainless steel chamber with 8 CF35 apertures on the side, one at the top and one at the bottom, as illustrated in Fig. 3.11. One of the openings is connected to a T nipple which connects to an angle valve and an ion pump to maintain the pressure of 5×10^{-10} Torr inside the science chamber. The opposite end is attached to an oven as a source for thermal atoms. A Hellma glass cell is connected to one opening and is the main science chamber of the system where the cloud of cold atoms will be transferred after the loading and cooling of thermal atoms in 3D-MOT is completed.

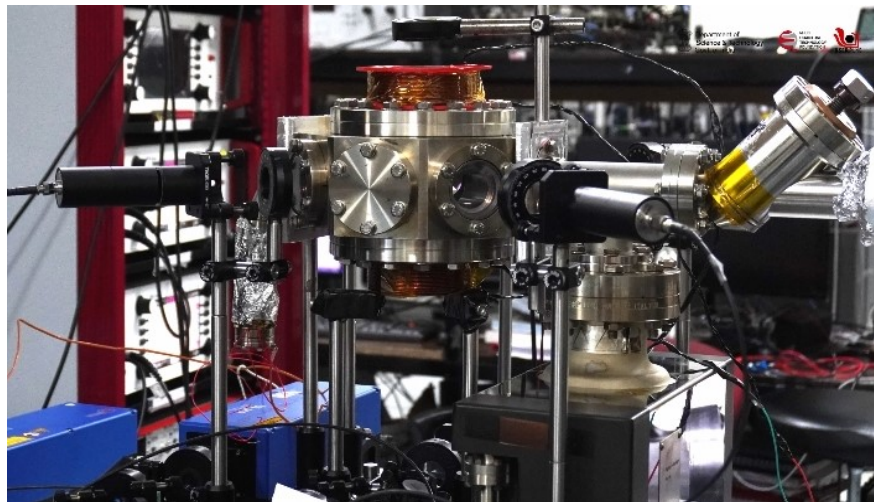


Figure 3.11: Experimental Setup of 3D-MOT

Toptica TA pro was used as the cooling laser for the 3D-MOT system; the laser was locked on transition frequency of transition $F = 2 \rightarrow F' = 2$ through the SAS technique, and the frequency stabilised laser beam was aligned to pass through an AOM operating at 128 MHz in double pass configuration that shifts the laser frequency by 256 MHz which is red-detuned by 10.650 MHz from the resonance frequency of transition $F = 2 \rightarrow F' = 3$. The beams are then split into two. One of them is used for confining the motion of atoms in the vertical direction, whereas the second beam is used to confine the atoms in the horizontal plane, as shown in Fig. 3.13. For optical repumping of the atoms which lost out of cooling cycle transition, Toptica DL pro locked at $F = 1 \rightarrow F' = 1$ transition frequency, frequency stabilised laser beam was aligned to pass through an AOM operating at 75 MHz in double pass configuration which shifts the laser frequency which is red-detuned by 6.947 MHz from the repumping transition $F = 1 \rightarrow F' = 2$, the optical bench layout is shown Fig. 3.12.

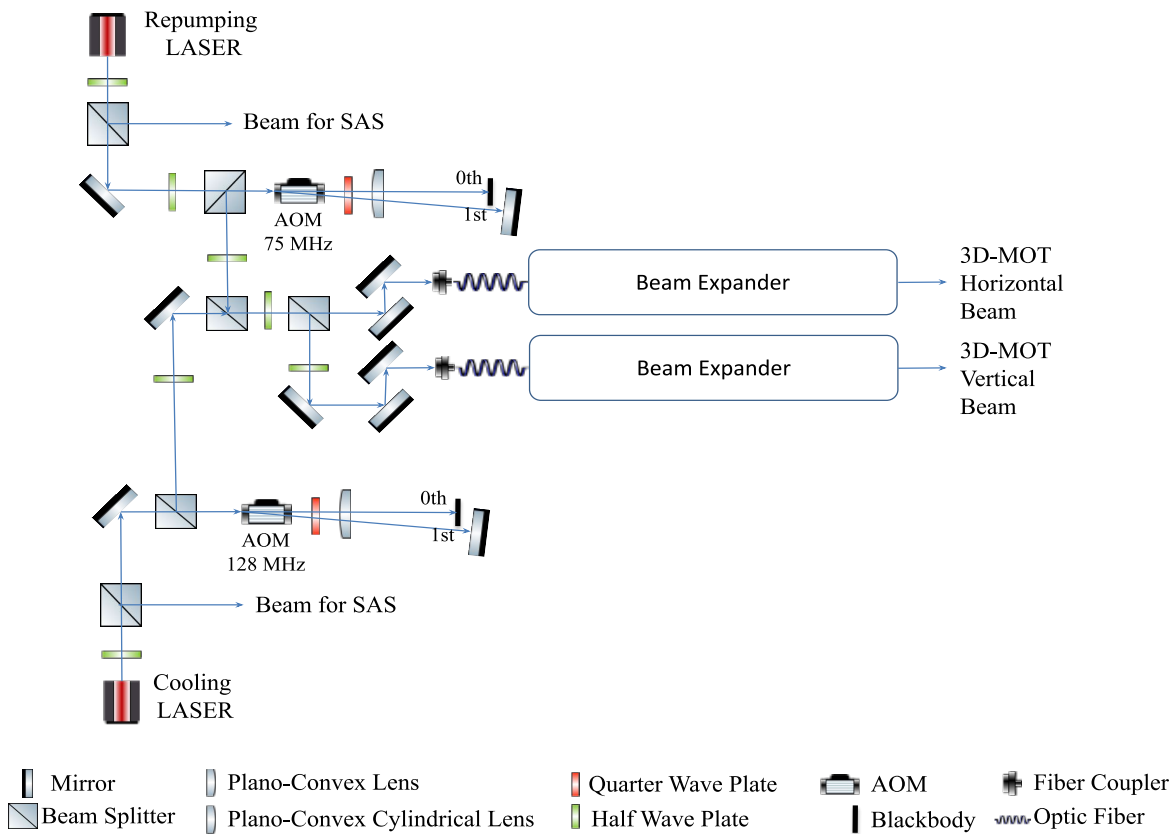


Figure 3.12: *Optical bench layout. Schematic of arrangement of optical components in the 3D-MOT experimental setup*

To generate the magnetic field, a pair of circular coils with diameters of 70 mm separated by 116 mm are used, as illustrated in Fig. 3.14. To find the ideal current for MOT loading, the coils were operated at three different currents: 4 A, 6 A, and 8 A, with corresponding constant magnetic field gradients of 11.90 G/cm, 17.85 G/cm, and 23.80 G/cm, as shown in Fig. 3.15.

For imaging MOT in the science chamber, a convex lens with a focal length of f is set at a distance of $2f$ from the cloud of cold atoms, and a photodiode is mounted on the other side of the lens at the same distance to record the fluorescence of the atoms in the MOT as shown in Fig. 3.16. This setup is known as the $2f - 2f$ configuration.

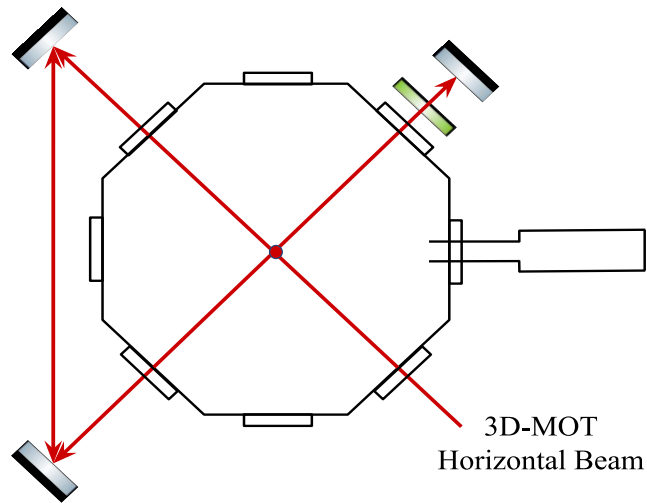


Figure 3.13: Top view of 3D-MOT science chamber

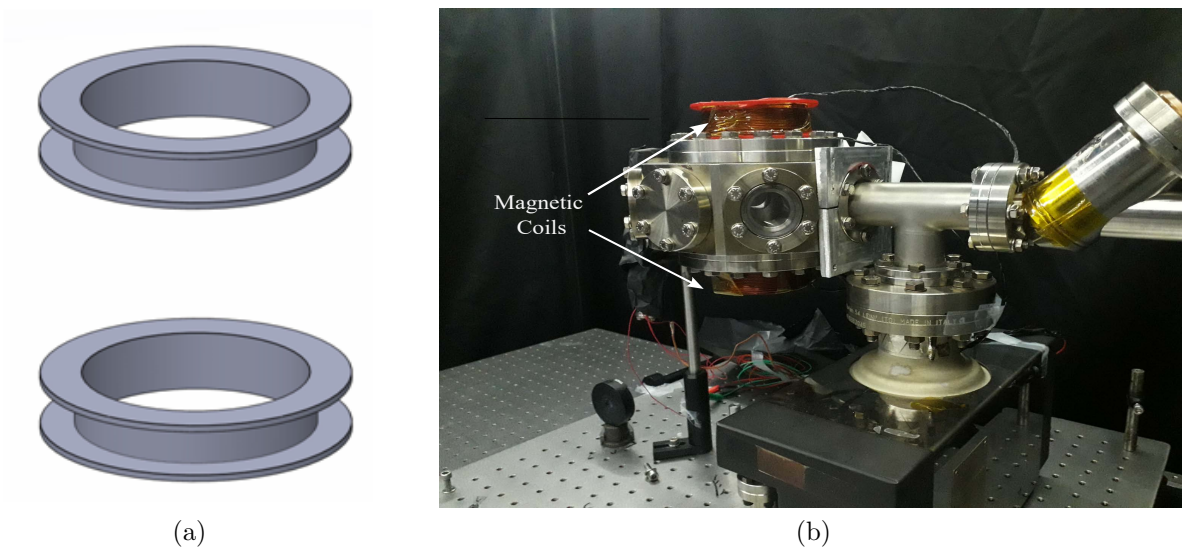
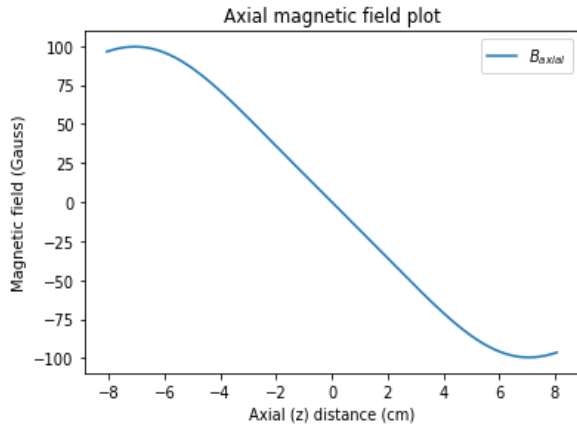
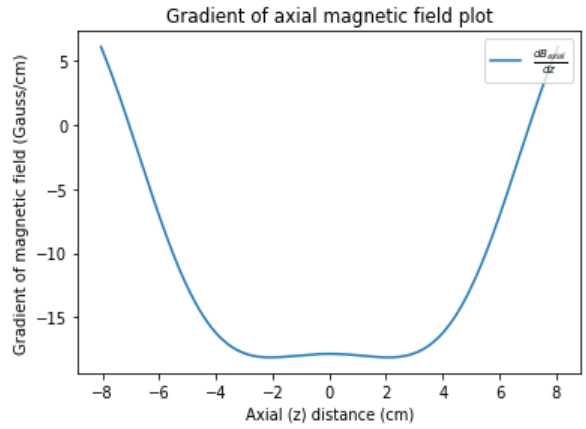


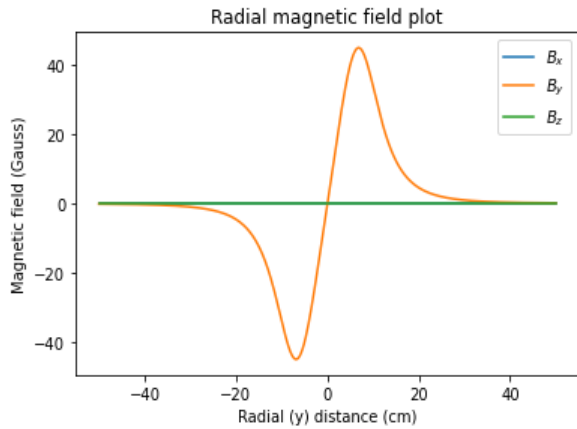
Figure 3.14: CAD model of magnetic coils used in 3D-MOT (a). Magnetic coils installed in the experimental setup (b)



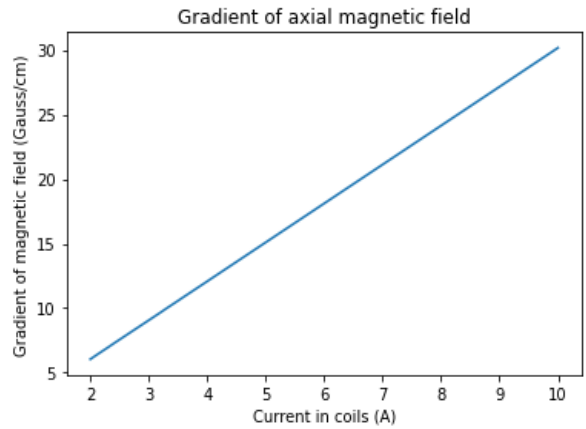
(a)



(b)



(c)



(d)

Figure 3.15: Magnetic field profile generated by magnetic coils operating at 6 A. (a) Magnetic field profile measured in the axial direction. (b) Magnetic field gradient profile in the axial direction. (c) Magnetic field profile along radial directions. (d) Constant magnetic field gradient for various values of current in the coils

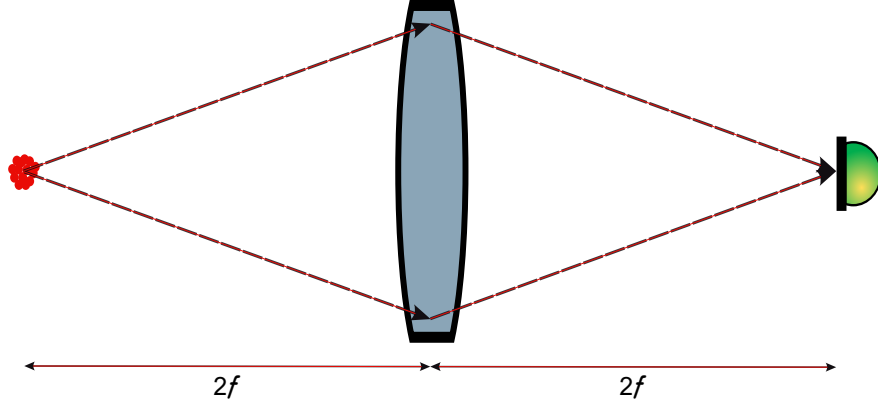


Figure 3.16: Schematics for Fluorescence imaging. A lens of focal length f is used to collect the light coming from the cloud of cold atoms onto a photodiode.

3.4 Experimental Setup of EIT

EIT experiments were carried out on a cloud of cold atoms in the 3D-MOT setup. A Toptica DL pro was used as the coupling laser to excite atoms from the $5^2P_{3/2}F' = 3$ state to higher energy states, as shown in Fig. 3.17. The absorption of the probe laser (780 nm) was reduced when the coupling laser interacted with the MOT; to monitor this effect, the same imaging approach used in 3D-MOT was used to image the MOT in the presence of the coupling laser beam and when the coupling laser beam was turned off. The fluorescence of MOT due to coupling laser was recorded on a photodiode.

The coupling laser was scanned over a frequency range of 10 MHz with a scan rate of 0.02 Hz for the Rydberg excited state spectroscopy. The cooling laser, repumping laser and magnetic field were kept on during experiments. The experiments were performed for three different Rydberg excited states, Fig. 3.18 shows the excitation scheme used in the experiments. The signal generated by the spectroscopy was used to frequency stabilise the coupling laser for the required transition.

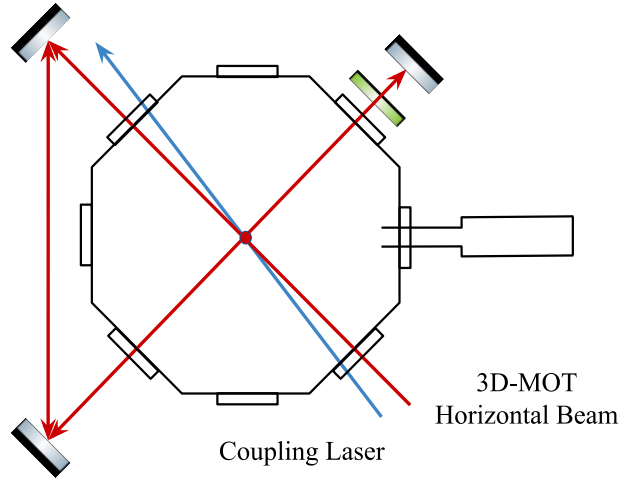


Figure 3.17: Top view of 3D-MOT science chamber and a coupling laser aligned to pass through MOT centre.

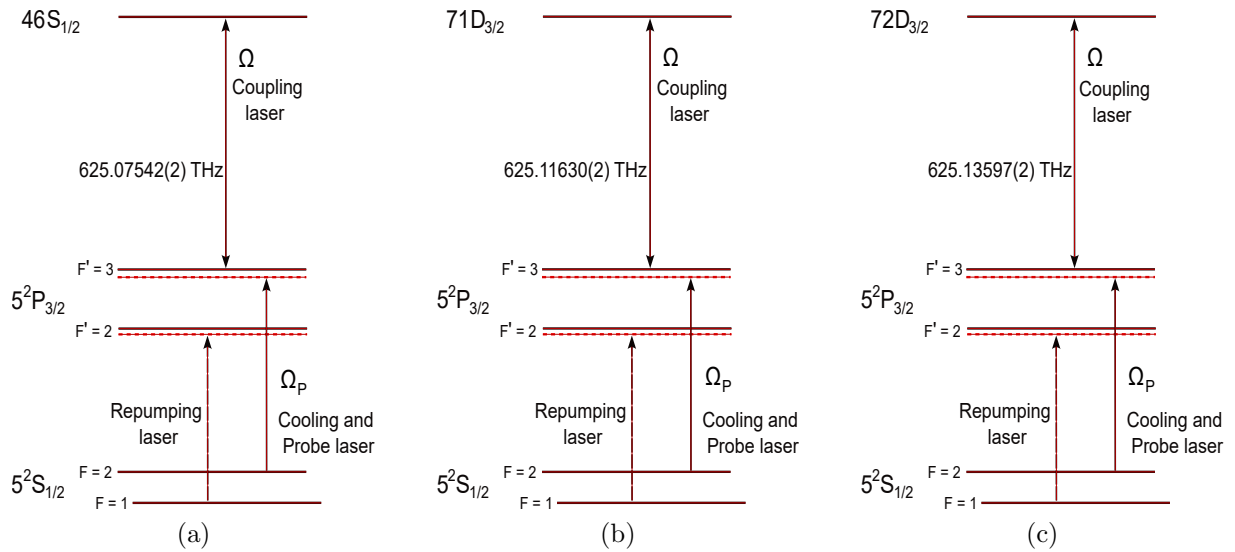


Figure 3.18: Excitation scheme for EIT experiments. (a) $5^2P_{3/2} \longleftrightarrow 46S_{1/2}$ in coupling laser frequency stabilisation experiment. (b) $5^2P_{3/2} \longleftrightarrow 71D_{3/2}$ transition to observe the reduction in fluorescence of the probe laser. (c) $5^2P_{3/2} \longleftrightarrow 72D_{3/2}$ transition used for Rydberg spectroscopy of $72D_{3/2}$ state

Experimental Results and Discussions

4.1 MOT Characterization

It is important to characterise MOT loading as it helps to optimise the system by comparing different MOT loading characteristic quantities such as MOT Loading Time, Number of Atoms and Decay rates are used. In this section, we will explore various parameters that impact MOT loading, and based on the results, we will determine which combination of parameters is most appropriate for operating MOT at maximum efficiency.

The image of the MOT was obtained on a Photo-Diode (using $2f - 2f$ configuration), which monitors the intensity of light falling on the sensor and produces a voltage corresponding to the intensity of the cloud of cold atoms. This data can be utilised to investigate the MOT Loading properties.

The number of atoms in a cloud is calculated using Eq. 4.1 [18].

$$P = \frac{hc}{\lambda} \frac{\Omega}{4\pi} NR_S \quad (4.1)$$

where P is the optical power, Ω is the solid angle subtended by the lens, N is the number of atoms in the cloud, and R_S is the scattering rate calculated from Eq. 2.5.

The MOT Loading rate equation is:

$$\frac{dN}{dt} = R - \frac{N}{\tau} - \beta \int n^2(r, N) d^3r \quad (4.2)$$

where N is the number of atoms at time t , R denotes the loading rate, $1/\tau$ denotes the linear loss rate, and the last term denotes the loss of atoms from the MOT due to light-assisted collision between the atoms in the MOT. The steady-state solution for Eq. 4.2 is:

$$N = \frac{R}{\Gamma + \beta \left(\int n^2(r, N) d^3r \right) / N} \quad (4.3)$$

A MOT Loading for multiple values of constant magnetic field gradient.

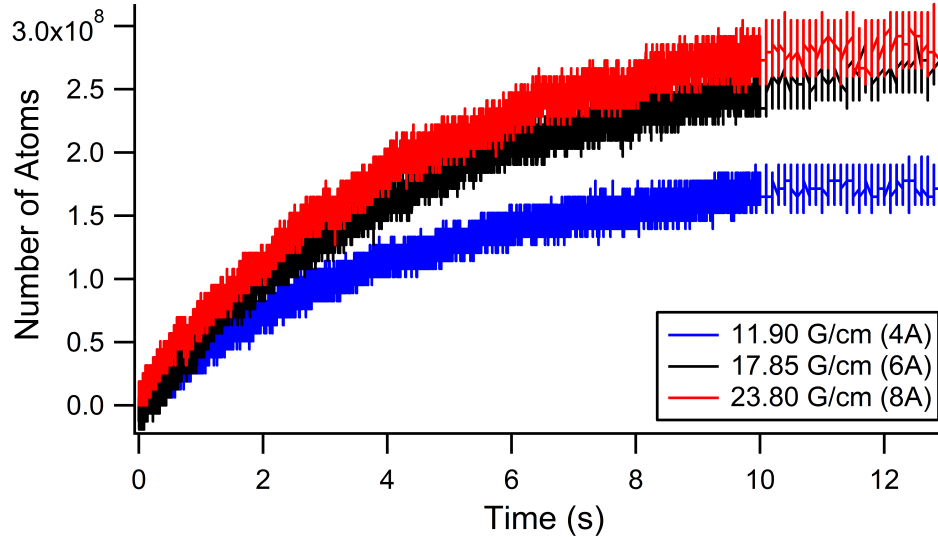


Figure 4.1: MOT loading curve for three different values of constant magnetic field gradient

| Sr. No. | Magnetic Field Gradient (G/cm) | Number of Atoms | Loading Rate (s) |
|---------|------------------------------------|--------------------|----------------------|
| 1 | 11.90 | 1.84×10^8 | 4.4 |
| 2 | 17.85 | 2.79×10^8 | 4.7 |
| 3 | 23.80 | 2.98×10^8 | 4.6 |

Table 4.1: MOT loading rate and Number of atoms in MOT calculated from Fig. 4.1

Fig. 4.1 shows the MOT loading for three different constant magnetic field gradient values. Ramping up the current in the coils from 4 A (11.90 G/cm) to 6 A (17.85 G/cm) increases the optical power (number of atoms) significantly, this is because as shown in Fig. 2.12, the Zeeman splitting is linear in the region with constant magnetic field gradient, for the given Doppler shifted laser frequency, the resonance transition frequency is controlled by changing the splitting of the Zeeman sublevel, and as the Doppler shifted laser frequency is near resonance to the desired frequency the light-matter interaction is maximum. Hence ramping up the current from 4 A to 6 A increases the number of atoms significantly, as at 6 A, the resonance frequency of the transition for a particular velocity class with maximum number of atoms is close to the laser frequency increasing the light-matter interaction. However, when the current in coils is increased from 6 A to 8 A (23.80 G/cm), the increase was small as compared to the previous situation because at 6 A velocity class with the maximum number of atoms where already on resonance, so ramping up current to 8 A increased the width of the velocity class, hence, increasing the number of atoms further.

B MOT loading for multiple Rb vapour background pressure values.

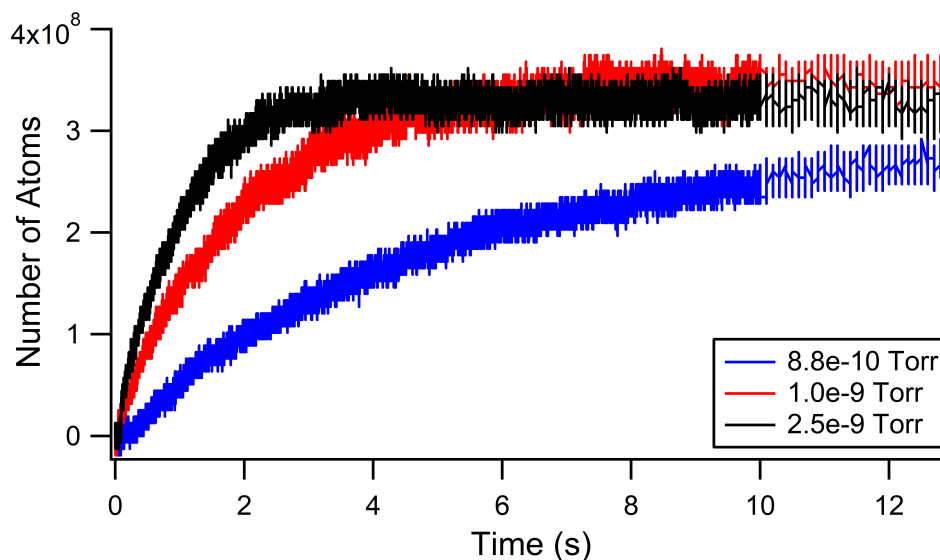


Figure 4.2: MOT loading curve for three different values of background pressure

Fig. 4.2 is MOT loading characteristics for three different background pressure of Rb vapour. In Fig. 4.2, the saturation point for all three pressure values is almost the same. However, the loading rate is different; the loading time is less for high background pressure

| Sr. No. | Pressure (<i>Torr</i>) | Number of Atoms | Loading Rate (<i>s</i>) |
|---------|--------------------------|--------------------|---------------------------|
| 1 | 8.8×10^{-10} | 2.79×10^8 | 4.8 |
| 2 | 1.0×10^{-9} | 3.55×10^8 | 1.9 |
| 3 | 2.5×10^{-9} | 3.30×10^8 | 0.9 |

Table 4.2: MOT loading rate and Number of atoms in MOT calculated from Fig. 4.2

and high for low background pressure. To understand this behaviour, we have to look at the rate equation of MOT loading, Eq. 4.2, R is the loading rate of the atom into MOT, and N/τ term is the loss rate of atoms from the trap due to collisions of trapped atoms with untrapped or thermal atoms. These terms are proportional to the pressure inside the science chamber due to Rb vapour. The last term in the Eq. 4.2 represents the loss of atoms from the trap due to collision between atoms inside the MOT, β in this term is the loss rate which depends on the intensity and detuning of the Cooling Laser and Repumping Laser, and $n(r, N)$ represent the total atom density distribution in the MOT. In our case, the number of atoms in the MOT $N > 10^6$ in the saturation, the contribution of the third term in the Eq. 4.2 is less, thus at high pressure, the number of atoms in the MOT tend to a maximum pressure-independent value $N_{lim} = R\tau$. As a result, all three curves saturate around the same point. However, when the number of atoms in MOT $N < 10^4$ third term of the equation is significant. [1, 10, 15].

This is because this setup uses background loading to load atoms in MOT, and raising Rb vapour pressure increases the number of thermal atoms in the velocity class that is trapped in the MOT.

C MOT Loading for multiple values of Cooling Laser intensity.

Fig. 4.3 is loading for three different power (intensity) of the cooling laser. For this experiment, the current in the magnetic coils was kept constant at 6 A, and the background pressure was 9.7×10^{-10} Torr. Fig. 4.3 shows increasing the intensity of the cooling laser increases the number of atoms in the MOT; however, the increase in the number of atoms is not linear with increasing intensity. This is because the force on the atom in MOT given by Eq. 2.4 depends on the scattering rate given in Eq. 2.5, for large values of I/I_{Sat} the second term of the Eq. 2.5 tends to 1. As a result saturation point for high-intensity trapping laser also saturates.

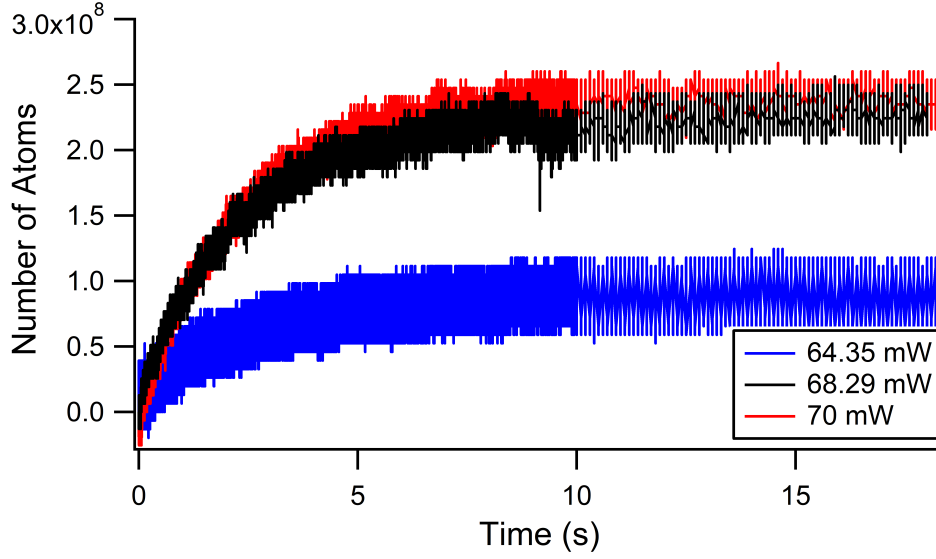


Figure 4.3: MOT loading curve for three different values of cooling laser intensity

| Sr. No. | Power (<i>mW</i>) | Number of Atoms | Loading Rate (<i>s</i>) |
|---------|---------------------|--------------------|---------------------------|
| 1 | 64.35 | 1.25×10^8 | 2.7 |
| 2 | 68.29 | 2.37×10^8 | 2.3 |
| 3 | 70 | 2.48×10^8 | 2.2 |

Table 4.3: MOT loading rate and Number of atoms in MOT calculated from Fig. 4.3

After analysing the data in Table 4.1, 4.2, and 4.3, optimal values for the 3D-MOT setup was decided. The magnetic coils are operated at 6 A of current because the heat in the magnetic coils was substantially high for currents above 6 A, and the increase in the number of atoms in the MOT was significantly less at currents less than 6 A. The pressure inside the 3D-MOT chamber is kept around 8.5×10^{-10} Torr, as operating at higher pressure reduced the loading time significantly and the number of atoms in MOT where high, but operating at high pressure limits the experimental abilities of the system.

4.2 Fluorescence Images of Cloud of Cold Atoms.

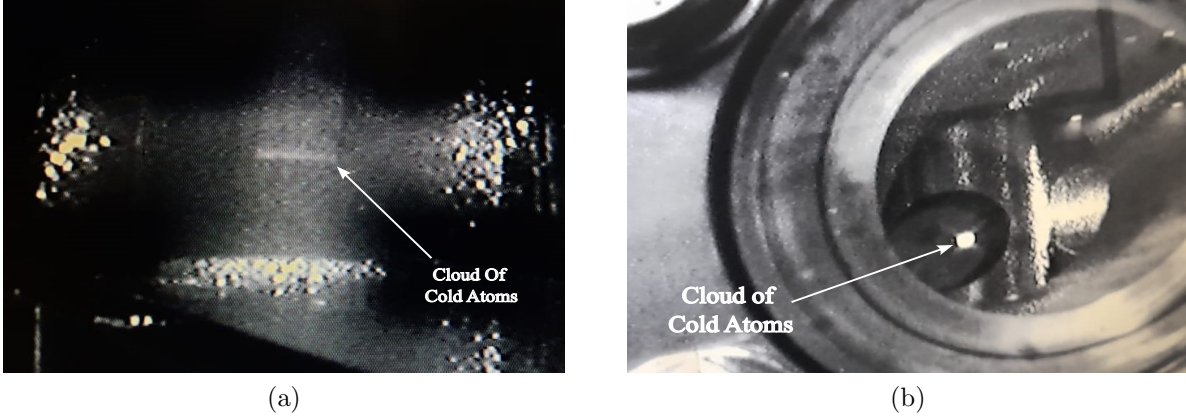


Figure 4.4: Fluorescence image of cloud of cold atoms. Atoms trapped in 2D-MOT (a). atoms trapped in 3D-MOT (b).

4.3 Electromagnetically Induced Transparency.

The EIT experiments reported in the thesis are *ladder*-type system, where the probe laser is the cooling laser of the 3D-MOT, which excites atoms from

$5^2S_{1/2} (F = 2) \rightarrow 5^2P_{3/2} (F' = 3)$, these two states are $|1\rangle$ and $|2\rangle$ states of the system as shown in Fig. 2.13, and $nS_{1/2}$ and $nD_{3/2}$ shown in Fig 3.18 are the highly excited Rydberg states represented by $|3\rangle$ in the Fig. 2.13.

4.3.1 EIT Signal. Reduction in Fluorescence of Probe Laser

Fig. 4.5 shows the reduction in fluorescence of probe laser exciting the atoms from $5^2S_{1/2} (F = 2) \rightarrow 5^2P_{3/2} (F' = 3)$ and a coupling laser operating at 625.11630 THz excites the atoms from $5P_{3/2} (F' = 3) \rightarrow 71D_{3/2}$ as shown in Fig. 3.18 [27]. Since this is a *ladder*-type system, the ρ_{12} from Eq. 2.50 has a non-zero value; hence reduction in the fluorescence of probe laser will never be complete (100%). However, that is not the case from the data recorded in Fig. 4.5; this is due to the sensitivity of the photodiode.

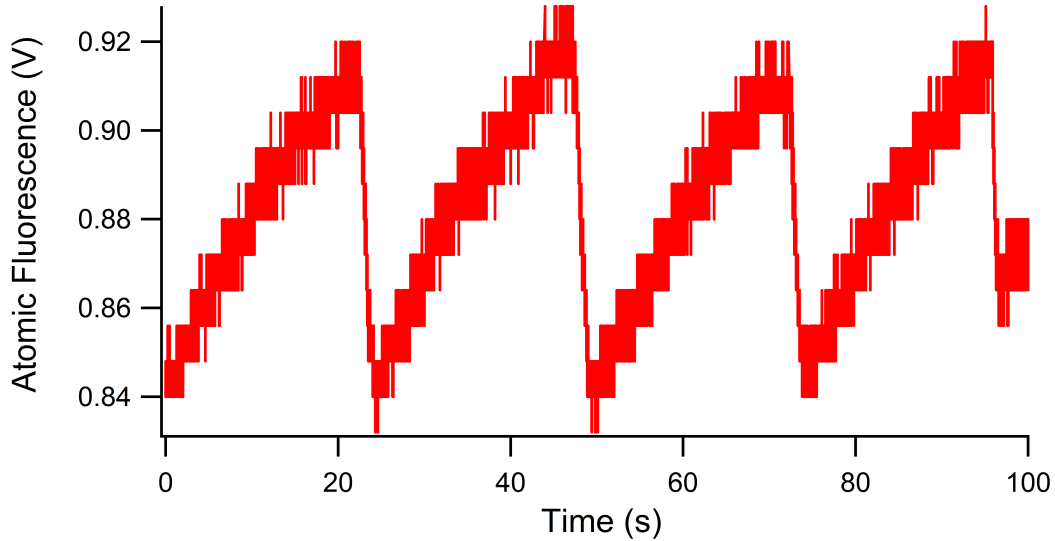


Figure 4.5: *First EIT signal.* Reduction fluorescence of probe laser due to coupling laser which excites atoms from $5P_{3/2} (F' = 3) \rightarrow 71D_{3/2}$.

During this experiment, the coupling laser was scanned over a frequency range of 10 MHz around the central frequency with a scan rate of 2 Hz. This spectroscopy of the $71D_{3/2}$ state should give a Lorentzian distribution which is not present in the Fig. 4.5. This is because a scan rate of 2 Hz is very fast for the spectroscopy of this energy level; in this setting, the laser is scanning 10 MHz in 0.5 s, and as a result, the resolution is not good enough to perform the spectroscopy of the $71D_{3/2}$ state and MOT loading characteristic dominate. With a slow scanning rate of 0.02 Hz and scan range of 10 MHz, a well-resolved spectroscopy is recorded in Fig. 4.6.

4.3.2 Spectroscopy of highly excited ($72D_{3/2}$) state

Fig. 4.6 is the spectroscopy of $72D_{3/2}$ state. For this experiment, fluorescence imaging of the MOT was done using a photodiode. Coupling laser with central frequency 625.13597 THz, was used for transition $5P_{3/2} (F' = 3) \rightarrow 72D_{3/2}$ as shown in Fig 3.18 [27], the laser was frequency scanning in 10 MHz range from the central frequency with a scan rate of 0.02 Hz, data is then fit using Lorentzian Function (black line in plot) and full-width half maxima (FWHM) for the fit is 3.52 MHz.

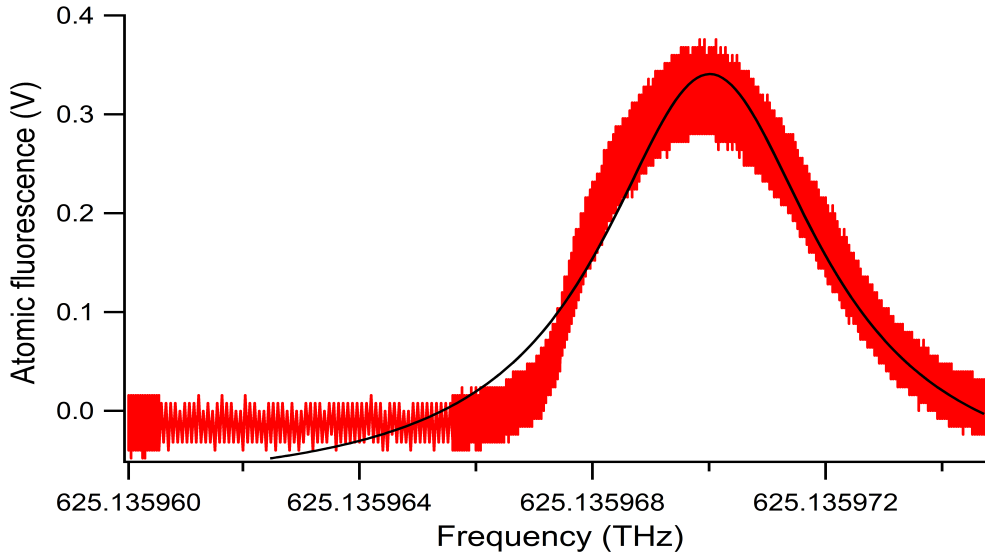


Figure 4.6: Spectroscopy of $72D_{3/2}$ state.

4.3.3 Frequency Stabilisation for $5^2P_{3/2}(F' = 3) \rightarrow 46S_{1/2}$ transition.

For frequency stabilisation of laser, atomic transition was used as a reference. The coupling laser was used to perform the spectroscopy of $5^2P_{3/2}(F' = 3) \rightarrow 46S_{1/2}$ transition shown in Fig 3.18 and the signal was given in PID (proportional–integral–derivative) for side-of-fringe locking. Fig. 4.7 shows the data (blue curve) given to PID for side-of-fringe locking

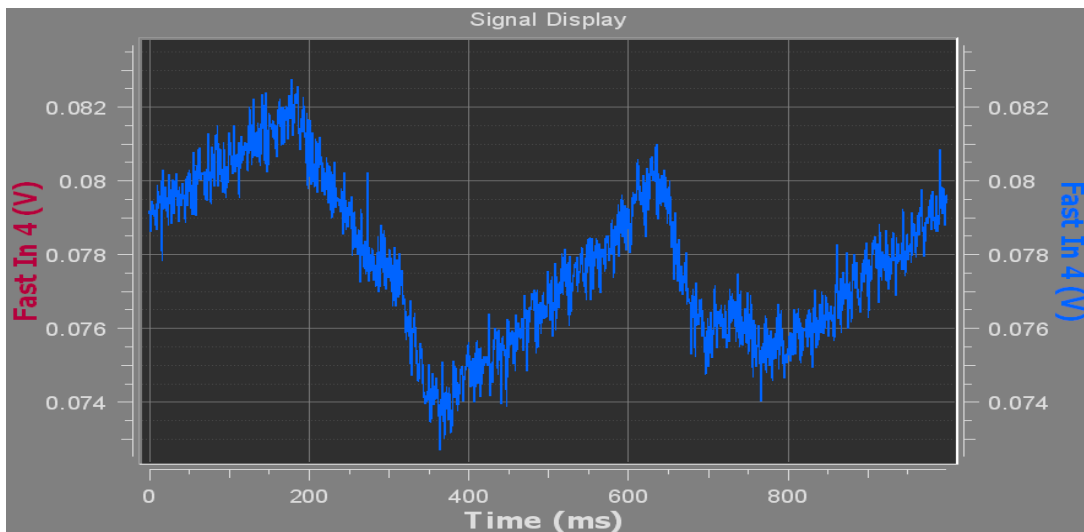


Figure 4.7: Screenshot of the signal (blue curve) given to PID for side-of-fringe locking

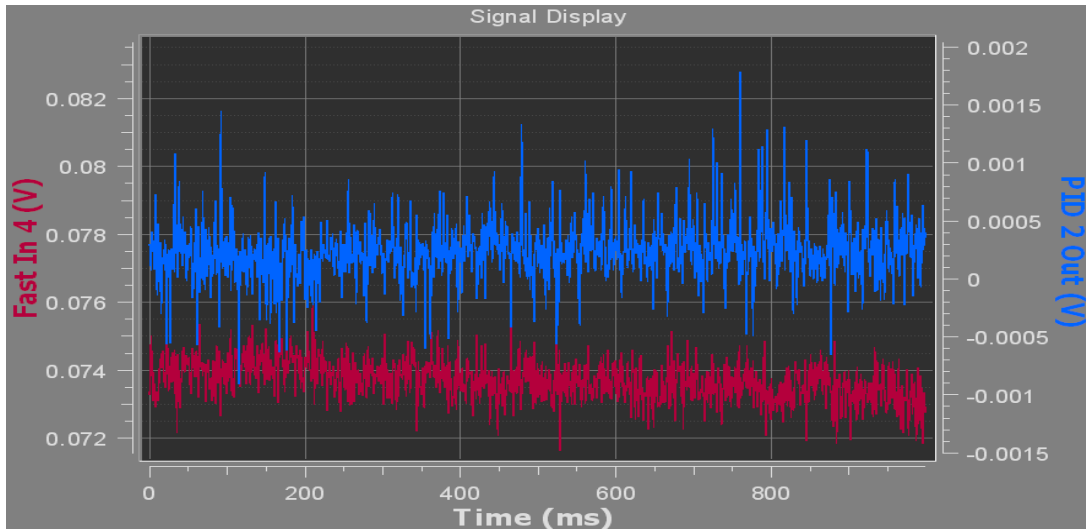


Figure 4.8: Output of the PID after locking (blue curve), and input signal from photodiode after locking laser (red curve)

After side-of-fringe locking, the coupling laser was locked on 625.07542 THz (479.61006 nm), which is the transition frequency for $5^2P_{3/2} (F' = 3) \rightarrow 46S_{1/2}$ shown in Fig. 4.8 where the input of PID (red curve) is constant, and Fig. 4.9 show the data from the wavemeter which measured the wavelength of the laser while it was locked to transition frequency for 20 ms, then it was unlocked, and the laser started scanning around the central wavelength (479.61006 nm).

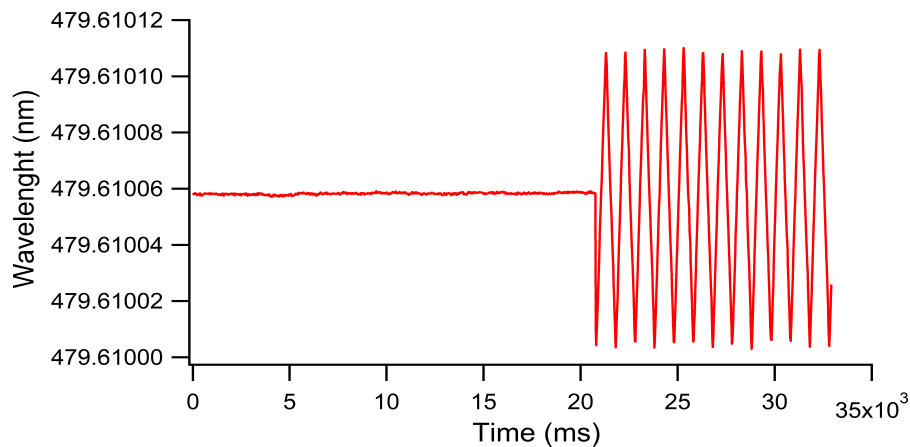


Figure 4.9: Data from Wavemeter. The laser was locked at the $5^2P_{3/2} (F' = 3) \rightarrow 46S_{1/2}$ transition frequency for 20 ms, then it was unlocked and began scanning about the set centre wavelength.

Summary and Outlook

5.1 Summary

The aim of this thesis is to develop compact 2D-MOT and 3D-MOT systems as a source of cold atoms to be used in various applications such as portable Atom-interferometer based gravimeters, Quantum Simulator and Quantum Information Processor. The work in the thesis can be divided in three parts. Development of 2D-MOT setup, development of 3D-MOT setup and to perform experiment of Electromagnetically Induced Transparency and Rydberg state of ^{87}Rb .

The experimental setup for 3D-MOT was studied in detail. Atoms in 3D-MOT are loaded from the background vapour of ^{87}Rb , we loaded $\sim 2.8 \times 10^8$ atoms in ~ 4.7 s, to achieve this result 6 A of current was applied to magnetic coils field to generate the constant magnetic field gradient of 17.85 G/cm, the total intensity in the MOT beams was 70 mW and the pressure inside the 3D-MOT chamber was 8.5×10^{-10} Torr. After, the loading of and cooling of atoms in 3D-MOT, Electromagnetically Induced Transparency experiment in the cloud of cold atoms was carried, where a *ladder*-type system was considered to observe EIT in cloud of cold atoms followed by spectroscopy of $72D_{3/2}$ Rydberg state. These signal from spectroscopy of excited were then used to frequency stabilize the coupling laser often called as Rydberg Laser in Quantum information processing.

5.2 Future Outlook

The current 3D-MOT setup has a quartz glass cell as the main science chamber. This chamber provides accessibility to perform various sophisticated experiments, the idea is to transfer the cloud of cold atoms from the 3D-MOT chamber to this glass chamber using a focused Gaussian beam dipole trap. Once transferred in this chamber cold atoms could be used for various experiments such as:

- **Neutral Atoms Array**

Tightly focused Gaussian beam optical tweezers that produce trapping potentials are used to load atoms from the MOT into specified lattice structures to perform various Quantum simulation and Quantum information processing experiments. The current setup's architecture is ideal for such research, and experiments with Rydberg State support the concept of developing the device into a portable Quantum Information Processor (QIP).

- **Quantum Gravimeters**

Quantum Gravimeters are absolute precision measuring instruments that use Atom-interferometry to measure g . Measurement of acceleration due to gravity g is crucial for various scientific research areas, making accurate measurement of g an essential necessity. By replacing the glass chamber with a longer glass chamber in the direction of measurement, the present set might be converted into a portable quantum gravimeter.

Bibliography

- [1] ANDERSON, M. H., PETRICH, W., ENSHER, J. R., AND CORNELL, E. A. Reduction of light-assisted collisional loss rate from a low-pressure vapor-cell trap. *Phys. Rev. A* 50 (Nov 1994), R3597–R3600.
- [2] BARREDO, D., LIENHARD, V., DE LESELEUC, S., LAHAYE, T., AND BROWAEYS, A. Synthetic three-dimensional atomic structures assembled atom by atom. *Nature* 561, 7721 (2018), 79–82.
- [3] BARWOOD, G. P., GILL, P., AND ROWLEY, W. R. C. Frequency measurements on optically narrowed rb-stabilised laser diodes at 780 nm and 795 nm. *Applied Physics B* 53 (1991), 142–147.
- [4] BIZE, S., SORTAIS, Y., SANTOS, M., MANDACHE TOMESCU, C., CLAIRON, A., AND SALOMON, C. High-accuracy measurement of the 87rb ground-state hyperfine splitting in an atomic fountain. *EPL (Europhysics Letters)* 45 (01 2007), 558.
- [5] BROWAEYS, A., BARREDO, D., AND LAHAYE, T. Experimental investigations of dipole–dipole interactions between a few rydberg atoms. *Journal of Physics B: Atomic, Molecular and Optical Physics* 49, 15 (jun 2016), 152001.
- [6] CHU, S., HOLLBERG, L., BJORKHOLM, J. E., CABLE, A., AND ASHKIN, A. Three-dimensional viscous confinement and cooling of atoms by resonance radiation pressure. *Phys. Rev. Lett.* 55 (Jul 1985), 48–51.
- [7] DALIBARD, J., AND COHEN-TANNOUDJI, C. Laser cooling below the doppler limit by polarization gradients: simple theoretical models. *J. Opt. Soc. Am. B* 6, 11 (Nov 1989), 2023–2045.
- [8] EBADI, S., WANG, T. T., LEVINE, H., KEESLING, A., SEMEGHINI, G., OMRAN, A., BLUVSTEIN, D., SAMAJDAR, R., PICHLER, H., HO, W. W., CHOI, S., SACHDEV, S., GREINER, M., VULETIĆ, V., AND LUKIN, M. D. Quantum phases of

- matter on a 256-atom programmable quantum simulator. *Nature* 595, 7866 (July 2021), 227–232.
- [9] FALLER, J. E., AND MARSON, I. Ballistic methods of measuring g - the direct free-fall and symmetrical rise-and-fall methods compared. *Metrologia* 25, 1 (jan 1988), 49.
- [10] FENG, P., HOFFMANN, D., AND WALKER, T. Comparison of trap-loss collision spectra for ^{85}Rb and ^{87}Rb . *Phys. Rev. A* 47 (May 1993), R3495–R3498.
- [11] FEYNMAN, R. P. Simulating physics with computers. In *Feynman and computation*. CRC Press, 2018, pp. 133–153.
- [12] FOX, M. *Quantum Optics*. Oxford University Press, 4 2006.
- [13] GRIMM, R., WEIDEMÜLLER, M., AND OVCHINNIKOV, Y. Optical dipole traps for neutral atoms. *Advances in Atomic, Molecular, and Optical Physics* 42 (12 2000), 95.
- [14] HAENSCH, T., AND SCHAWLOW, A. Hänsch, t. w. schawlow, a. l. cooling of gases by laser radiation. opt. commun. 13, 68-69. *Optics Communications* 13 (01 1975), 68–69.
- [15] HOFFMANN, D., FENG, P., AND WALKER, T. Measurements of rb trap-loss collision spectra. *J. Opt. Soc. Am. B* 11, 5 (May 1994), 712–720.
- [16] KASEVICH, M., AND CHU, S. Measurement of the gravitational acceleration of an atom with a light-pulse atom interferometer. *Applied Physics B* 54 (1992), 321–332.
- [17] KRZYSZTOF, K., XUAN, K. D., MAŁGORZATA, G., HUY, B. N., JERZY, S., ET AL. Magneto-optical trap: fundamentals and realization. *CMST*, 2 (2010), 115–129.
- [18] KUMAR, S. *Towards Distributed Quantum Information Processing Using Coupling Of Neutral Atoms to Plasmonic Nanostructures*. PhD thesis, Dept. of Physics, 2017.
- [19] LETT, P. D., WATTS, R. N., WESTBROOK, C. I., PHILLIPS, W. D., GOULD, P. L., AND METCALF, H. J. Observation of atoms laser cooled below the doppler limit. *Phys. Rev. Lett.* 61 (Jul 1988), 169–172.
- [20] LÖW, R., WEIMER, H., NIPPER, J., BALEWSKI, J. B., BUTSCHER, B., BÜCHLER, H. P., AND PFAU, T. An experimental and theoretical guide to strongly interacting rydberg gases. *Journal of Physics B: Atomic, Molecular and Optical Physics* 45, 11 (may 2012), 113001.
- [21] MIGDALL, A. L., PRODAN, J. V., PHILLIPS, W. D., BERGEMAN, T. H., AND METCALF, H. J. First observation of magnetically trapped neutral atoms. *Phys. Rev. Lett.* 54 (Jun 1985), 2596–2599.

- [22] OHL DE MELLO, D., SCHÄFFNER, D., WERKMANN, J., PREUSCHOFF, T., KOHFAHL, L., SCHLOSSER, M., AND BIRKL, G. Defect-free assembly of 2d clusters of more than 100 single-atom quantum systems. *Phys. Rev. Lett.* *122* (May 2019), 203601.
- [23] PAIK, H., BLASER, J.-P., AND VITALE, S. Principle of the step accelerometer design. *Advances in Space Research* *32*, 7 (2003), 1325–1333. Fundamental Physics in Space.
- [24] PHILLIPS, W. D., AND METCALF, H. Laser deceleration of an atomic beam. *Phys. Rev. Lett.* *48* (Mar 1982), 596–599.
- [25] PROTHERO JR, W., AND GOODKIND, J. A superconducting gravimeter. *Review of Scientific Instruments* *39*, 9 (1968), 1257–1262.
- [26] RAAB, E. L., PRENTISS, M., CABLE, A., CHU, S., AND PRITCHARD, D. E. Trapping of neutral sodium atoms with radiation pressure. *Phys. Rev. Lett.* *59* (Dec 1987), 2631–2634.
- [27] S., S. B., BARIK, S. K., CHAUDHURI, S., AND ROY, S. Transition frequency measurement of highly excited rydberg states of 87rb for a wide range of principal quantum numbers. *Opt. Continuum* *1*, 5 (May 2022), 1176–1192.
- [28] SAFFMAN, M., WALKER, T. G., AND MØLMER, K. Quantum information with rydberg atoms. *Rev. Mod. Phys.* *82* (Aug 2010), 2313–2363.
- [29] STECK, D. Rubidium 87 d line data.
- [30] YAN, M., RICKEY, E. G., AND ZHU, Y. Electromagnetically induced transparency in cold rubidium atoms. *JOSA B* *18*, 8 (2001), 1057–1062.